

Calibration of a star formation and feedback model for cosmological simulations with Enzo

Boon Kiat Oh,¹^{*} Britton D. Smith,^{1,2} John A. Peacock,¹ and Sadegh Khochfar¹

¹*Institute for Astronomy, University of Edinburgh, Royal Observatory, Edinburgh EH9 3HJ, United Kingdom*

²*San Diego Supercomputer Center, University of California, San Diego, 10100 Hopkins Drive, La Jolla, CA 92093*

10 February 2020

ABSTRACT

We present results from seventy-one zoom simulations of a Milky Way-sized (MW) halo, exploring the parameter space for a widely-used star formation and feedback model in the Enzo simulation code. We propose a novel way to match observations, using functional fits to the observed baryon makeup over a wide range of halo masses. The model MW galaxy is calibrated using three parameters: the star formation efficiency (f_*), the efficiency of thermal energy from stellar feedback (ϵ) and the region into which feedback is injected (r and s). We find that changing the amount of feedback energy affects the baryon content most significantly. We then identify two sets of feedback parameter values that are both able to reproduce the baryonic properties for haloes between $10^{10} M_\odot$ and $10^{12} M_\odot$. We can potentially improve the agreement by incorporating more parameters or physics. If we choose to focus on one property at a time, we can obtain a more realistic halo baryon makeup. We show that the employed feedback prescription is insensitive to dark matter mass resolution between $10^5 M_\odot$ and $10^7 M_\odot$. Contrasting both star formation criteria and the corresponding combination of optimal feedback parameters, we also highlight that feedback is self-consistent: to match the same baryonic properties, with a relatively higher gas to stars conversion efficiency, the feedback strength required is lower, and vice versa. Lastly, we demonstrate that chaotic variance in the code can cause deviations of approximately 10% and 25% in the stellar and baryon mass in simulations evolved from identical initial conditions.

Key words: cosmology:theory – galaxies:formation – galaxies:evolution – galaxies:haloes

1 INTRODUCTION

The large-scale structure of the universe can be understood quite precisely by considering models that consist purely of dark matter. Numerical simulations of structure formation in such models have been performed with high accuracy and progressively higher resolution and larger box size (Efstathiou et al. 1985; Moore et al. 1999; Springel et al. 2008; Diemand et al. 2008; Klypin et al. 2011). But on the baryonic side, limitations in numerical resolution mean that several baryonic processes are not simulated from first principles. These processes include fundamental phenomena of the transformation of cold gas to stars, feedback from the energy released by stars, supernovae and massive black holes. Such effects are implemented using a subgrid approach in cosmological hydrodynamical simulations (Springel & Hernquist

2003; Governato et al. 2010; Agertz et al. 2013; Shimizu et al. 2019). If these analytical implementations are too simplistic, they risk being sensitive to poorly determined parameters, thus limiting their capability to make robust predictions. Improving the accuracy of subgrid physics requires both a better understanding of physical processes and identification of their limitations.

Feedback processes are essential in order to solve fundamental issues in numerical simulations such as the ‘overcooling problem’ (Cole 1991; White & Frenk 1991; Blanchard et al. 1992) and the ‘angular momentum problem’ (Katz & Gunn 1991; Navarro & White 1994; Hummels & Bryan 2012). Overcooling results in the formation of too massive galaxies particularly in high-resolution simulations (Davé et al. 2001). Feedback is also important for shaping the density profile of dark matter haloes (Pontzen & Governato 2012; Martizzi et al. 2013; Davis et al. 2014). In addition to these issues of small-scale subgrid physics, cosmological

* E-mail: bkoh@roe.ac.uk

simulations contain additional uncertainties. In the absence of feedback, Genel et al. (2018) highlighted differences in the properties of galaxies induced by very slight changes in the initial positions of dark matter particles. Even if a galaxy is evolved from identical initial conditions, the simulation code can introduce variances which result in fluctuations in the simulated properties between repetitions of the same simulation (Keller et al. 2019). The problem is alleviated by the self-regulating nature of feedback (Keller et al. 2019) and highlights the need to understand the impact that subgrid implementations have on the resulting properties of galaxies in simulations.

Feedback processes that inject energy into the gas are therefore integral to numerical simulations. For smaller mass haloes, the energy comes mainly from supernovae explosions. In contrast, for more massive ones, the main energy sources are active galactic nuclei (AGN) (Sijacki et al. 2007; Booth & Schaye 2009; Teyssier et al. 2011) and gravitational heating as a result of infalling clumps of matter (Dekel & Birnboim 2006; Khochfar & Ostriker 2008). However, it is unclear how the energy should be distributed between generating motion and heating the gas. For supernova feedback alone, various techniques have been employed across different simulation codes (Stinson et al. 2006; Cen & Ostriker 2006; Dubois & Teyssier 2008; Dalla Vecchia & Schaye 2012; Smith et al. 2018). Given the huge diversity in the method of implementation, it is not unusual to expect significantly different outcomes (Thacker & Couchman 2000; Springel & Hernquist 2003; Okamoto et al. 2005; Oppenheimer & Davé 2006; Schaye et al. 2010), and variation in feedback effects is the most significant source of uncertainty in a cosmological simulation. In particular, the role of resolution should be emphasised: the resolution in cosmological simulations is limited but feedback occurs on all scales, so rigorous numerical convergence cannot be expected. The subgrid parameterisation, or at least the subgrid parameter values, will need to change according to the resolution in order to match calibrating observations, and there is no guarantee that all predicted galaxy properties will then be independent of resolution.

To reproduce a realistic picture of the observed universe, there is thus a need to calibrate the parameters of the appropriate subgrid routines (Schaye et al. 2015). These are adjusted to match specific observational properties of the galaxy population. By matching related properties, the simulation can then be used to answer a wide range of questions. For example, the feedback implementation in the ‘Evolution and Assembly of GaLaxies and their Environments’ (EAGLE) simulation project is calibrated to reproduce the observed $z = 0.1$ galaxy stellar mass function (GSMF), the relation between the mass of galaxies and their central black holes and realistic galaxy sizes (Schaye et al. 2015). The Illustris group calibrate their parameters to match various observational scaling relations and galaxy properties at low and intermediate redshifts (Vogelsberger et al. 2014). Despite the calibrations, there are shortcomings in each simulation. For example, Illustris recognised that the decrease of their simulated cosmic star formation rate density was too slow, leading to an update in their feedback prescription, resulting in the introduction of IllustrisTNG (Pillepich et al. 2018).

In contrast to these full cosmologically representative

box simulations, zoom simulations focus computational resources on smaller volumes (Springel et al. 2008; Griffen et al. 2016; Wang et al. 2015). In particular, Wang et al. (2015) studied a halo mass range from dwarf masses ($5 \times 10^9 M_\odot$) to Milky Way (MW) masses ($2 \times 10^{12} M_\odot$). They included baryonic processes and were able to reproduce the stellar to halo mass relation from abundance matching (Behroozi et al. 2013b; Moster et al. 2013; Kravtsov 2013) across a wide range of redshifts. However, they did not account for the mass of gas remaining in the haloes, and this is an important issue for the present analysis.

In this paper, we use zoom simulations of MW haloes in an attempt to quantify the stellar and gas mass present in such a halo at $z = 0$. In particular, we examine the degree of calibration allowed by the model introduced by Cen & Ostriker (1992). Although newer models are available, the Cen & Ostriker model remains as one of the most highly-used models in Enzo simulations. We calibrate our parameters governing star formation and feedback via a comparison with the inventory of baryonic and gravitating masses of cosmic structures presented in McGaugh et al. (2010), in particular the mass fraction of baryons in the halo and the conversion efficiency of gas into stars. Not only is this the first suite of simulations using these observables for feedback calibration, it tests how well the Cen & Ostriker (1992) model can be calibrated.

This paper is structured as follows. Section 2 describes the generation of initial conditions used in the simulations, the code, and setup used to evolve them. Also, we describe the parameters used for calibration and analysis tools used to extract and analyse the results. Section 3 presents the properties from McGaugh et al. (2010) that we attempt to match, along with the observational fit of the Kennicutt–Schmidt relation (Kennicutt et al. 2007). Section 4 describes the results from various simulations: effects of single parameter variation, calibration of parameters to results from McGaugh et al. (2010) and performance of the simulations to match other constraints. Lastly, the results are summarised and discussed in Section 5.

2 SIMULATION SETUP AND ANALYSIS

This section provides an overview of the simulation setup and the associated subgrid physics. In particular, the focus is on a MW-sized halo, at which mass scale we expect that AGN feedback will be subdominant (Bower et al. 2006; Behroozi et al. 2010; Stocchi-Bergmann 2014). The main parameters investigated will thus be related to star formation efficiency and supernova feedback, and one aim of this investigation is indeed to see to what extent we can reproduce the baryonic properties of the MW using solely these ingredients. As described by Crain et al. (2015), the resulting baryonic properties of the halo are very sensitive to the variations of feedback parameter values. Therefore, a detailed explanation of the role of each parameter in the physical model is necessary.

The cosmological parameters in this suite of simulations are taken from WMAP-9 (Bennett et al. 2013). The key parameters are $\Omega_m = 0.285$, $\Omega_\Lambda = 0.715$, $\Omega_b = 0.0461$, $h = 0.695$ and $\sigma_8 = 0.828$ with the usual definitions. With these parameters, we generate initial conditions with MULTI-scale Initial

Conditions (MUSIC) for cosmological simulations (Hahn & Abel 2011). We derive all zoom simulations from the parent simulation with a volume of $L = 100 h^{-1} \text{cMpc}$ with 256^3 particles.

The simulation is evolved using **Enzo**, an adaptive mesh-refinement (AMR) code (Bryan et al. 2014). **Enzo** uses a block-structured AMR framework (Berger & Colella 1989) to solve the equations of hydrodynamics in an Eulerian frame using multiple solvers. In the simulations presented here, we use the **ZEUS** (Stone & Norman 1992) hydro solver in combination with an N-body adaptive particle-mesh gravity solver (Efsthathiou et al. 1985). Parameter space exploration is performed mainly on the star formation and feedback routines; the results of this exploration will be outlined extensively in Section 2.1 and 2.2. Lastly, the chemistry and cooling processes are handled by the **Grackle** library (Smith et al. 2017). We use the equilibrium cooling mode from **Grackle**, which utilises the tabulated cooling rates derived from the photoionisation code **CLOUDY** (Ferland et al. 2013) together with the UV background radiation given by Haardt & Madau (2012).

The MW-sized halo is initially identified from a dark matter only parent simulation through its merger history and final dark matter halo mass. It is isolated, has not experienced a major merger in its merger history since at least $z = 2$ and has a final mass of approximately $10^{12} M_{\odot}$. The particles within a high-resolution region, typically larger than the virial radius, then undergo additional levels of refinement in mass while the region’s spatial resolution is increased. Each nested level is equivalent to an increase in spatial and mass resolution by a factor of two and eight, respectively. Contamination occurs if larger mass particles cross the region of interest (Oñorbe et al. 2014). In our simulations, we define a high-resolution region of three virial radii from the centre of the halo to carry out the refinement (Simpson et al. 2018) as a preventive measure. We use three nested levels, giving an effective resolution of 2048^3 particles or a nested dark matter particle mass of $1.104 \times 10^7 M_{\odot}$. This nested simulation is evolved with an additional five levels of AMR which is only allowed around particles within the high-resolution region, resulting in a maximum resolution of eight levels of spatial refinement or 2.196 comoving kpc (ckpc). This simulation setup is similar to that presented by Peebles et al. (2019) and Hummels et al. (2018).

From the high-resolution region of the MW halo, we identify an additional smaller halo with a mass of approximately $10^{10} M_{\odot}$. We then run a separate simulation zooming in only on this halo with two additional levels of initial nesting. The purpose of this smaller halo is to test the universality of the optimal feedback parameters from the MW zoom simulation. Due to the additional nesting levels, the dwarf is made up of approximately the same number of dark matter particles as in the MW halo. The increased mass resolution translates into an effective resolution of 8192^3 particles or a nested dark matter particle mass of $1.715 \times 10^5 M_{\odot}$. Because of the additional nested levels, we reduce the number of AMR levels to three, maintaining a constant maximum spatial resolution of 2.196 ckpc.

2.1 Star formation parameters

This paper employs the model described by Cen & Ostriker (1992) with modifications for the purpose of calibration. This model is one of the most commonly used in **Enzo**. The conditions required for star formation in a cell include:

- (i) No further refinement within the cell
- (ii) Gas density greater than a threshold density: $\rho_{\text{gas}} > \rho^{\text{threshold}}$
- (iii) Convergent flow: $\nabla \cdot \mathbf{v} < 0$
- (iv) Cooling time less than a dynamical time: $t_{\text{cool}} < t_{\text{dyn}}$
- (v) Gas mass larger than the Jeans mass: $m_{\text{gas}} > m_{\text{jeans}}$
- (vi) Star particle mass is greater than a threshold mass

If all the conditions are fulfilled, the algorithm generates a ‘star particle’ within the grid cell with a mass

$$m_* = m_{\text{gas}} \times \frac{\Delta t}{t_{\text{dyn}}} \times f_*, \quad (1)$$

where m_{gas} is the gas mass in the cell, Δt is the timestep, t_{dyn} is the dynamical time and f_* is a dimensionless efficiency factor. The mass of the generated star particle is compared to a user-defined minimum star particle mass. If the mass exceeds the threshold, a star particle will be created. It is positioned in the centre of the cell and possesses the same peculiar velocity as the gas in the cell. It is treated dynamically as all other particles. An equivalent mass of gas to that of the star particle is then removed from the cell to ensure mass conservation.

To calibrate the simulation, certain aspects of the star formation criteria are modified. These include the Jeans instability check, time dependence of star formation, threshold stellar mass and the value of f_* . The following sections will explain the role that each parameter plays: they are organized in the order that each factor is used in the star formation condition check.

2.1.1 Jeans instability check

In item (v) of the list of conditions in Section 2.1, the creation of star particles is only allowed when the gas mass exceeds the Jeans mass of the cell. This criterion is aimed at low resolution simulations that cannot resolve local Jeans masses. However, modern implementations with better resolution resolve such clouds with multiple cells at the star formation threshold density. When the spatial resolution of the simulation is high enough to resolve the Jeans length, this particular check in the star formation routine instead restricts star formation that can occur because an individual cell needs to wait until enough mass has accumulated within it.

2.1.2 Minimum star particle mass

Once a cell fulfils all five conditions for star formation, the final barrier to star formation is the minimum mass of a star particle that will be inserted into the simulation. This threshold is explicitly designed to prevent the production of too many star particles, which can increase computational costs significantly. However, the inability to exceed this minimum star particle mass can lead to a build-up of poten-

Table 1. List of the star formation setups explored

Star formation setup list			
Setup	Jeans instability check	Minimum star particle mass [M_{\odot}]	Timestep dependence of star formation
1	✓	10^5	✓
2	✗	0	✗

tial star-forming gas in surrounding cells. This accumulation then reaches a point where a burst in star formation occurs.

2.1.3 Timestep dependence of star formation

Two factors affect the mass of the star particle to be compared to the threshold value as seen in Equation 1: $\Delta t/t_{\text{dyn}}$ and f_* . They correspond to the timestep dependence of star formation and a conversion factor respectively. The $\Delta t/t_{\text{dyn}}$ factor aims to explicitly satisfy the Kennicutt–Schmidt (KS) relation, which states that a fraction f_* will turn into stars over a dynamical time. However, this factor is introduced at multiple points in the star formation process, which impedes the promptness of star formation and its associated feedback by only converting a limited amount of gas into stars. By opting for a timestep independent star formation, the factor $\Delta t/t_{\text{dyn}}$ is removed from the calculation shown in Equation 1, resulting in a stellar mass of

$$m_* = m_{\text{gas}} \times f_*, \quad (2)$$

where the symbols have the same meaning as in Equation 1. In this timestep independent approach, the simulation instantaneously converts f_* of gas into stars in each timestep and the associated feedback will immediately start regulating further star formation. This modification greatly improves the efficiency of the star formation and feedback processes but requires further adjustments as discussed in detail in later sections.

As we show in Sections 4.2 and 4.3, the timestep independent star formation model generally leads to a smoother buildup of stellar mass, but not without some additional effects. When we contrast the performance of the simulation, a simulation employing timestep dependent star formation will take roughly a month to complete whereas a similar setup with timestep independent star formation completes in approximately two days, reflecting the production of fewer star particles. Shorter run times allow for more exploration of the parameter space. However, this choice has significant impact on the resulting KS relation. These effects will be quantified and discussed in Section 4. In summary, we calibrate the feedback in two different star formation setups as detailed in Table 1. The reasons for two setups will be discussed in Section 4.3.

2.1.4 Star formation efficiency factor, f_*

As mentioned, regardless of the timestep dependence of star formation, there exists an efficiency factor, f_* , in both Equations 1 and 2. This parameter regulates the conversion efficiency of identified gas mass in a cell into star particles: f_* can vary from zero to unity but not including the limits where none or all the identified gas mass in the cell is converted to stellar mass respectively. The latter scenario will

remove all the gas from the cell, resulting in a cell having a density of zero, crashing the simulation.

2.2 Feedback parameters

Although the creation of a star particle is immediate, feedback happens over a longer timescale, designed to mimic the gradual process of star formation. In each timestep, the star forming mass is given by

$$m_{\text{form}} = m_0 \left[\left(1 + \frac{t - t_0}{t_{\text{dyn}}} \right) \exp \left(-\frac{t - t_0}{t_{\text{dyn}}} \right) - \left(1 + \frac{t + dt - t_0}{t_{\text{dyn}}} \right) \exp \left(-\frac{t + dt - t_0}{t_{\text{dyn}}} \right) \right], \quad (3)$$

where m_0 is the star particle mass, t_0 and t are the creation time of the star particle and current time in the simulation respectively. Through this implementation, according to Equation 3, the rate of star formation increases linearly and peaks after one dynamical time before declining exponentially (Smith et al. 2011).

We adopt the Smith et al. (2011) modification of the Cen & Ostriker (2006) thermal supernova feedback model. The star particles add thermal feedback to a set of neighbouring grids with size and geometry that can be tuned by the user, known as distributed stellar feedback. This feedback continues until 12 dynamical times after its creation. In each timestep, feedback is deposited in the form of mass, energy, and metals.

Mass is removed from the star particle and returned to the grid as gas, given by

$$m_{\text{ej}} = m_{\text{form}} \times f_{\text{ej}}, \quad (4)$$

where f_{ej} is the fraction of mass removed. The momentum of this gas is

$$p_{\text{feedback}} = m_{\text{ej}} \times v_{\text{particle}}, \quad (5)$$

where v_{particle} is the velocity of the star particle and is conserved by addition into the grid cell hosting the star. The feedback energy deposited into the user defined cells is

$$E_{\text{feedback}} = m_{\text{form}} \times c^2 \times \epsilon, \quad (6)$$

where ϵ and c are the feedback efficiency and speed of light respectively. For an ϵ value of 10^{-5} (Cen & Ostriker 1992), an energy of 10^{51} erg is injected for every $\sim 56 M_{\odot}$ of stars formed. Metals are returned to the grid cells and their corresponding metallicity is given by

$$Z_{\text{feedback}} = m_{\text{form}} \times ((1 - Z_{\text{star}}) \times \eta + f_{\text{ej}} \times Z_{\text{star}}), \quad (7)$$

where Z_{star} and η are the star particle metallicity and the fraction of metals yielded from the star respectively.

We assume that 25% of the mass is removed from the star particle and returned to the grid as gas ($f_{\text{ej}} = 0.25$) with 10% of this returned gas being metals ($\eta = 0.1$), consistent with Cen & Ostriker (1992). These values result in a total metal yield of 0.025 of the mass of the star particle, similar to the calculations by Madau et al. (1996). Also, this metal yield is consistent with average values in the MW, with a mean SFR of $\sim 3 M_{\odot} \text{ yr}^{-1}$, a core-collapse supernova rate of 1 per 40 years, and an IMF-averaged metal yield of $\sim 3 M_{\odot}$

per supernova (Smith et al. 2011). Therefore, we leave the values of both f_{ej} and η unaltered.

Instead, we focus on the factors that influence the energy injection, both in terms of the amount and the physical extent. We select three factors in the feedback implementation to be varied for the calibration of the simulations. They are ϵ , radius of feedback (r) and number of cells (s) within r . The first parameter is related to the amount of feedback energy emitted by the star particle (see Equation 6) while the remaining parameters work together to define the extent of energy injection. These will be described in more detail in the following sections.

2.2.1 Feedback efficiency, ϵ

The amount of feedback energy injected as thermal energy is given by Equation 6. It is dependent on both rest mass energy ($m_{\text{form}} \times c^2$) and a user-defined fraction, ϵ . The former relies on the amount of stellar mass created per timestep (see Equation 3), and the latter defines the percentage of the rest mass energy injected into the IGM. Together with Equation 4, this implementation is similar to the temporal release of Galactic Superwind energy and ejected mass from stars into the IGM discussed in Cen & Ostriker (2006).

2.2.2 Feedback energy injection extent

In the original feedback method described by Cen & Ostriker (2006), all of the feedback energy is injected into the grid cell housing the star particle. However, Smith et al. (2011) modified this to allow the feedback to be spread across multiple zones as a means of bypassing the overcooling issues, where too much energy injected into a single grid cell can result in unphysical short cooling times. This setup is known as distributed stellar feedback, and it is described by r and s . These parameters work together to define the physical extent of the injection of feedback from the star particle. We can visualise it in terms of a cube surrounding the star particle in the centre. r is the distance of the cell from the star particle. When $r = 1$, it refers to a 3×3 cube since all the cells are within one cell distance away from the star particle. Similarly, when $r = 2$, it refers to a 5×5 cube around the star particle. These alternatives are illustrated in two dimensions in the left and right panel of Figure 1 respectively.

The parameter s gives the number of steps allowed to be taken from the star particle within the cube determined by r . Referring to the left panel of Figure 1, setting $s = 2$ corresponds to an allowable two steps of movement away from the star particle, specifying injection within the cells labelled 1 and 2 in the 3×3 cube. As the value of r increases, shown in the right panel of Figure 1, so the maximum accessible value of s increases. These increased values translate to more flexibility in the usage of distributed stellar feedback.

In summary, we calibrate our simulations with ϵ , r and s , and f_* to match the observations. For the remainder of the paper, when discussing the combination of parameters in a simulation setup, they will be referred to as a vector with components (ϵ , r - s , f_s), e.g., $(1.0 \times 10^{-5}, 1.3, 0.1)$.

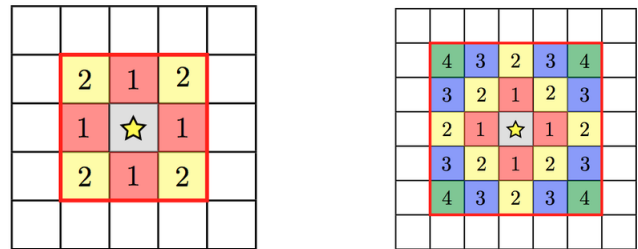


Figure 1. Schematics of the distributed stellar feedback setup for $r = 1$ (left) and $r = 2$ (right) (Enzo Collaboration 2018). Different coloured cells illustrate the accessible s corresponding to the particular value of r . For example, if $r = 1$, the maximum allowable value of s is 3 and it corresponds to an injection of feedback energy into a 3×3 cube. For a detailed explanation, refer to Section 2.2.2.

Table 2. Methods of determining V_c for different gravitationally bound systems (see McGaugh (2005); Hoekstra et al. (2005); Gavazzi et al. (2007); Walker et al. (2007, 2009); Simon & Geha (2007); Giodini et al. (2009)).

Gravitationally bound systems	Methods
Stellar dominated spiral galaxies	Rotation velocities
Gas dominated galaxies	Baryonic Tully-Fisher relation
Elliptical galaxies	Gravitational lensing
Local group dwarfs	Direct measurement
Clusters of galaxies	Hot X-ray emitting gas

2.3 Analysis

Haloes are identified using the Robust Overdensity Calculation using k-Space Topologically Adaptive Refinement (ROCKSTAR) halo finder (Behroozi et al. 2013a). It is a 6-dimensional phase-space finder, using both positions and velocities of particles to locate and define a halo. In regions where the density contrast is insufficient to distinguish which halo hosts a given particle, ROCKSTAR can differentiate sub-haloes and major mergers that are close to the centres of their host haloes. This feature is particularly useful in identifying main haloes when creating zoom simulations of lower mass haloes. Analysis of the simulation results is then carried out using the yt analysis toolkit (Turk et al. 2011).

3 OBSERVATIONAL CALIBRATIONS

3.1 Baryon content of cosmic structures

The main observables matched in this suite of simulations are taken from the work of McGaugh et al. (2010), where the authors attempted to quantify the distribution of baryonic mass within cosmic structures. Galaxies are broadly categorised into rotationally supported and pressure supported systems. These are further divided into stellar dominated spiral galaxies and gas dominated galaxies for the rotationally supported system, and elliptical galaxies, local group dwarfs and some clusters of galaxies for pressure supported systems. The primary method for determining the total mass budget in the different systems is their equivalent circular velocity (V_c) obtained through various methods described in detail in McGaugh et al. (2010) and summarised in Table 2.

In their analysis, McGaugh et al. (2010) chose to present

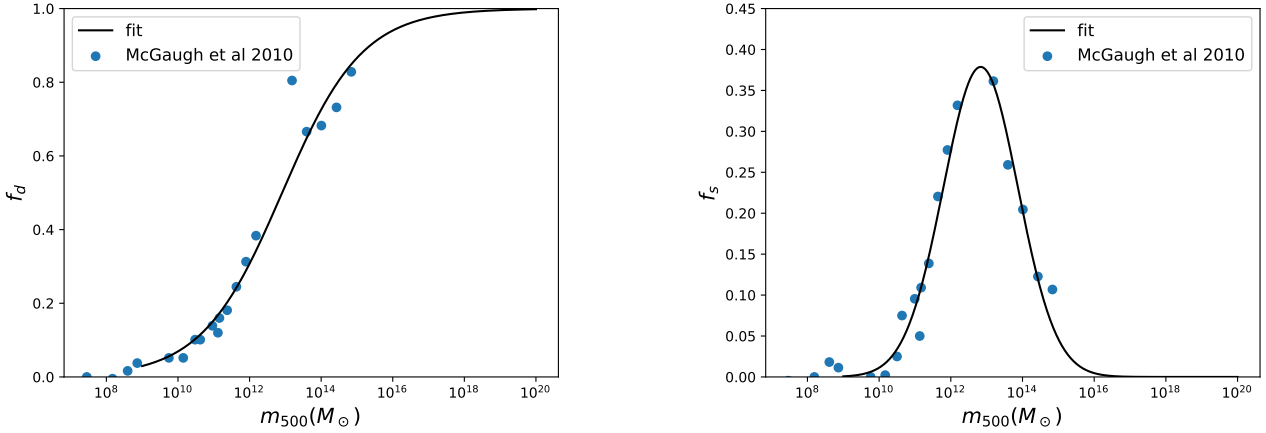


Figure 2. Best fit of the baryon fraction relative to the expected global fraction, f_d (left) and the fraction of those expected baryons in the form of stars, f_s (right) from [McGaugh et al. \(2010\)](#) with Equations 10 and 11 respectively.

their results using r_{500} , a radius where the enclosed density is 500 times the critical density of the universe. The main result presented in Figure 2 of [McGaugh et al. \(2010\)](#) relates the fraction of expected baryons that are detected,

$$f_d = \frac{m_b}{f_b \times m_{500}}, \quad (8)$$

and the conversion efficiency of baryons into stars,

$$f_s = \frac{m_*}{f_b \times m_{500}}, \quad (9)$$

where m_b and m_{500} refer to the baryonic and total mass within this radius respectively, and f_b is the universal baryon fraction determined to be 0.17 ± 0.01 ([Komatsu et al. 2009](#)). One important point to note is that these fractions are dependent on the choice of radius. To facilitate comparison of our results with this paper, we produced the following fitting formula to the data from Figure 2 in [McGaugh et al. \(2010\)](#), which we illustrate in Figure 2:

$$f_d = \frac{1}{1 + e^{-x}}, \quad (10)$$

and

$$f_s = 0.91 \exp\left(\frac{-y^2}{2}\right) \times f_d, \quad (11)$$

where

$$x = \frac{\log_{10}(m_{500}/M_\odot) - 12.91}{1.12}, \quad (12)$$

and

$$y = \frac{\log_{10}(m_{500}/M_\odot) - 12.19}{1.18}. \quad (13)$$

We aim to calibrate our suite of simulations to yield a good match to these fits. Also, we will compare our simulated galaxy properties to the Kennicutt–Schmidt relation, which serves as an additional constraint.

3.2 Kennicutt–Schmidt relation

The KS relation is a measure of the correlation between gas surface density and the SFR per unit area. From the work

of [Schmidt \(1959\)](#); [Kennicutt \(1989, 1998\)](#); [Kennicutt et al. \(2007\)](#); [Bigiel et al. \(2008\)](#), there appears to be a tight correlation between these measured properties on galactic scales (\sim kpc). This strong relation makes it one of the critical observations that simulations with star formation attempt to match.

We adopt a similar methodology to that of the AGORA project ([Kim et al. 2016](#)). The SFRs are calculated using the mass of star particles and time-averaged over the past 20 Myrs of the simulation snapshot. Together with the gas density they are then deposited onto a fixed resolution grid of 750 pc, consistent with the methodology of [Bigiel et al. \(2008\)](#), to derive the SFR and gas surface density required by the KS relation. In fact, we find that the conclusions drawn are insensitive to changes in the grid resolution. With non-zero SFR surface density patches, we will also compare our results to

$$\log \Sigma_{\text{SFR}} = 1.37 \log \Sigma_{\text{gas}} - 3.78, \quad (14)$$

which is obtained from the best observational fit given by Equation 8 in [Kennicutt et al. \(2007\)](#).

4 RESULTS

4.1 MW galaxy zoom simulations with Setup 1

We explore the parameter space by switching on the Jeans instability check, applying timestep dependent star formation and setting a threshold star particle mass of $10^5 M_\odot$ (Setup 1); see Table 1. With this setup, we run a total of 22 simulations by modifying f_* (see Equation 1), ϵ (see Equation 6), r and s (see Section 2.2.2), as shown in Figure 3. This explored region of parameter space is motivated both physically and numerically. [Cen & Ostriker \(1992\)](#) applied a value of ϵ ($10^{-4.5}$), which is similar to other work ([Ostriker & Cowie 1981](#); [Dekel & Rees 1987](#)). The values of r and s are restricted by the maximum number of cells used to define a grid. Lastly, we can constrain the range of values that f_* can take with the ratio of f_s to f_d . From [McGaugh et al. \(2010\)](#),

f_* is limited between 0.1 and 0.9 approximately across the halo mass range.

Out of the 22 simulations, we classify the runs into those that reached $z = 0$ (completed) and those that did not (failed) since we are interested in the relevant properties at $z = 0$. A fraction of the simulations were unable to reach the final redshift due to unrecoverable errors in the hydrodynamics solver, mostly associated with extreme star formation and/or feedback parameters. Since the failed simulation contains extreme feedback parameters, e.g. large amount of feedback energy, it is unlikely that this prescription will result in the best match to the observed properties, presented in Section 4.1.1. Overlapping points with conflicting conclusions exist in Figure 3 because as we are showing the 2-dimensional projection of the 3-dimensional parameter space.

4.1.1 Comparison to baryonic properties from *McGaugh et al. (2010)* – Setup 1

Initially, we attempted to cover the parameter space optimally with minimal numbers of simulations using Latin Hypercube Sampling (*McKay et al. 1979*). We wanted to minimise the maximal distance between various points in our feedback parameter space as described by *Heitmann et al. (2009)*. However, due to the failure of several runs to reach $z = 0$, it is not possible to obtain a space-filling design. Therefore, we try a more fundamental approach to quantify how changing each parameter will affect the observables. This result is presented in Figure 4, showing a plot of f_s against f_d across a range of m_{500} .

From the initial values of $(1.0 \times 10^{-5}, 1.3, 0.1)$, we vary ϵ only, which corresponds to a change in the strength of feedback. Increasing the strength of feedback reduces both the f_s and f_d parameters of the halo (see the blue arrow in Figure 4). This evolution can be easily explained by the increased expulsion of gas due to stronger feedback, reducing the amount of fuel available to form stars, which leads to a decrease in f_s . The removal of gas also causes the amount of baryons within r_{500} or f_d to decrease.

We then try to increase f_* . This change has a direct impact on the total stellar mass as more gas mass is converted into stars. However, this increased star formation yields stronger feedback. Therefore, the net result of increasing f_* is similar to increasing ϵ , which decreases both f_s and f_d (see the green arrow in Figure 4). To a lesser extent, however, this effect is evident from the small transition of the cyan point to the purple point on the top right of the plot. To improve the clarity of an increase in f_* , we add another green arrow connecting another set of data points (grey and light green dots). This difference in the impact of f_* also suggests its sensitivity to other feedback parameters.

The last parameters to adjust are r and s . Essentially, we are increasing the size of the cube into which the feedback energy is injected (see Figure 1). By increasing r (and, correspondingly, s), f_s and f_d are reduced, similarly to the effect of increasing ϵ and f_s . However, this phenomenon only persists until $r = 3$ and $s = 9$, which corresponds to a 7^3 box or 343 cells centred around the star particle. Beyond this point, the trend changes when a further extension of the feedback injection decreases f_s but increases f_d , indicating the presence of a turnaround point. As energy is deposited

further from the star particle, the gas is kept away at a larger distance from the centre of the gravitational potential well as seen in Figure 5. As a result, m_* decreases as fewer stars form due to a deprivation of fuel for star formation while m_{gas} increases as more gas is now present. Increasing the physical extent of feedback injection beyond $r = 3$ and $s = 9$ only serves to dilute the amount of feedback energy per cell, leading to gas remaining near the virial radius of the halo. Thus f_d increases while f_s decreases. Furthermore, the average number of cells within a single grid in an *Enzo* simulation is not likely to be much larger than about 7^3 , so extending beyond $r = 3$ and $s = 9$ should be avoided as feedback is only deposited on the local grid.

From the 16 completed simulations, the combination of parameters that yielded the most MW-like properties in the halo is $(2.5 \times 10^{-4}, 1.3, 0.2)$, which is represented by the pale green dot in Figure 4. The halo contains a stellar mass comparable to the MW while having approximately 50% more baryon mass than the MW halo. This point is the closest match to the target for the region of parameter space that we sampled. The next best set of parameters that produce halo properties matching the target is $(5.0 \times 10^{-4}, 1.3, 0.1)$. While it provides a better f_d agreement, the value of f_s is approximately zero. From the trends and the best match in Figure 4, further improvement in the agreement of halo properties will only be marginal. In order to achieve a better agreement, we suggest including other free parameters or even modifying the star formation and feedback model. Furthermore, this set of parameter is determined for a quiescent halo as discussed earlier. Success of this calibrated feedback prescription is likely to be dependent on the growth history as well. However, it is not within the scope of this work to design such modifications or test the robustness of our calibration against different merger histories.

4.1.2 Kennicutt–Schmidt relation – Setup 1

As discussed earlier, the KS relation provides an additional constraint on the feedback calibration beyond the global baryon makeup of a MW halo. To apply this constraint, we use the methodology described in Section 3.2 to compare and contrast with the observed KS relation (blue line) in Figure 6. We also include a rough approximation of the observed values of nearby galaxies from *Bigiel et al. (2008)* in the form of blue hatched contours.

The results show that the simulation data intersect with observations and the fit given by Equation 14, but the slopes of the simulation data differ from the KS relation in every feedback prescription. Most of our simulations manage to reproduce the characteristic ‘threshold’ gas density value of approximately $10 \text{ M}_{\odot} \text{ pc}^{-2}$, which marks the transition point between high and low star formation efficiency and is apparent from the blue hatched contour. The slopes of the relations in the simulations do not appear to be significantly different from each other despite changes in the subgrid physics parameters. However, they are consistently steeper than the gradient of the observed relation.

When increasing ϵ , we observe a shift towards lower SFR but higher gas density from the transition between the green circles $(1.0 \times 10^{-5}, 1.3, 0.1)$ and the red squares $(5.0 \times 10^{-4}, 1.3, 0.1)$. This shift can be explained by the higher feedback energy budget associated with a larger ϵ

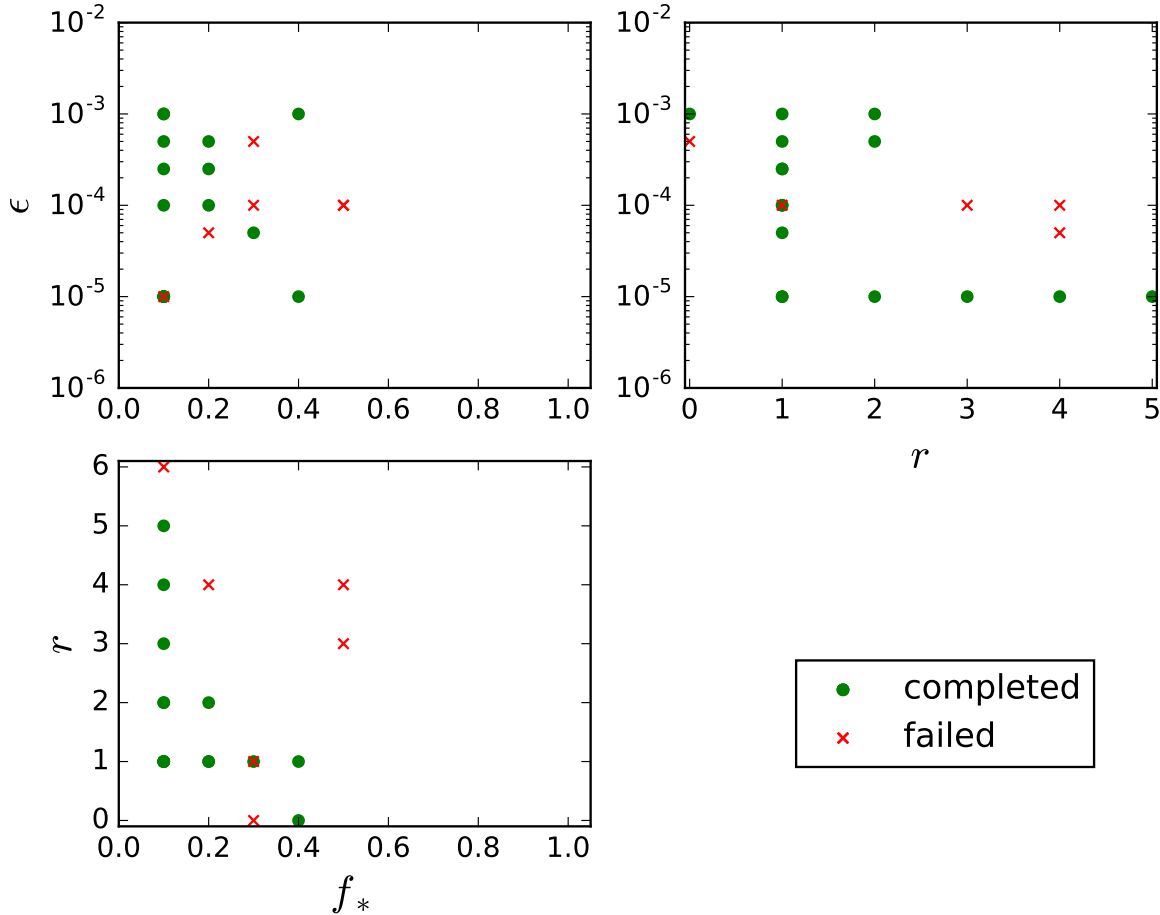


Figure 3. Overview of parameter space exploration using a total of 22 different combinations of f_* , ϵ and r with Setup 1. The plots are ϵ against f_* (top left), ϵ against r (top right) and r against f_* (bottom left). The green dots and red crosses represent runs that reached and failed to reach $z = 0$ respectively. We can identify regions of parameter space more likely to result in the inability of the simulation to reach $z = 0$ and the causes are explained in more detail in Section 4.1.

value, which inhibits further star formation. The simulation data points are insensitive to any increase in r until $r = 3$. Beyond which, comparable SFR densities are associated with higher gas densities (compare green crosses ($r = 4$) and pink diamonds ($r = 5$)). This trend is consistent with the explanation provided for Figure 5. Lastly, from the data points of $(1.0 \times 10^{-5}, 1.3, 0.1)$ and $(1.0 \times 10^{-5}, 1.3, 0.2)$, it appears that increasing f_* does not affect the relation significantly.

The best parameter values (purple hexagon) lie along with the KS relation fit but deviate from observations as they are clustered around high gas densities. This discrepancy with Bigiel et al. (2008) suggests that this combination of ϵ and f_* is too weak to create patches of lower gas surface density. However, adjustment of either factor will, in turn, affect f_s and f_d , leading to a halo that reproduces the KS relation instead of the observations of McGaugh et al. (2010).

4.1.3 Haloes in the high-resolution region – Setup 1

Since we specify a safety factor of three virial radii to prevent contamination of the MW halo in the zoom simulation, there are other central and satellite haloes of varying mass in this region. Figure 7 illustrates the properties of other central haloes in the simulation with the best feedback prescription of $(2.5 \times 10^{-4}, 1.3, 0.2)$. This plot is not presented in a similar way to Figure 4 because we are looking at a range of halo masses. Instead, we populate Figure 2 with the corresponding f_s and f_d of various central haloes in the high-resolution region of the MW galaxy zoom simulation.

We present the graph of f_d against m_{500} on the upper panel and f_s against m_{500} on the lower panel of Figure 7. The black lines are Equations 10 and 11 fitted to the observations (blue dots). From the graph of f_s on the lower panel, the properties either match observation well or do not form stars at all ($f_s = 0$), which is represented by a red star and grey cross respectively. The same cannot be said for the f_d relation on the left where there are vastly different properties with no apparent relation to the f_d values. We see lower mass haloes with f_d reaching 1.4, exceeding that of the uni-

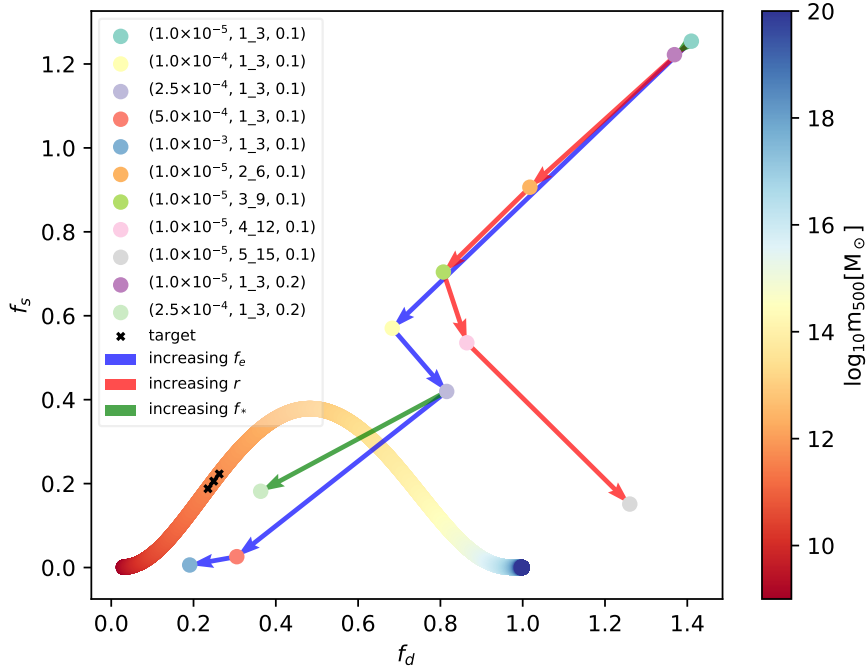


Figure 4. Graph of the stellar mass fraction f_s against the detected baryon fraction f_d across a range of m_{500} . The colour coded curve shows the values of f_s and f_d corresponding to the mass range indicated. Cross marks on this curve show the values to be matched. It includes the mean of m_{500} with the upper and lower limits given by the maximum and minimum m_{500} from the simulations plotted. Dots represent simulation with different feedback parameters and contrasting coloured arrows show effects of increasing a particular parameter. From the ensemble of simulations, $(2.5 \times 10^{-4}, 1.3, 0.2)$ yielded the most realistic baryonic makeup for the simulated MW galaxy. For a detailed description, refer to Section 4.1.1.

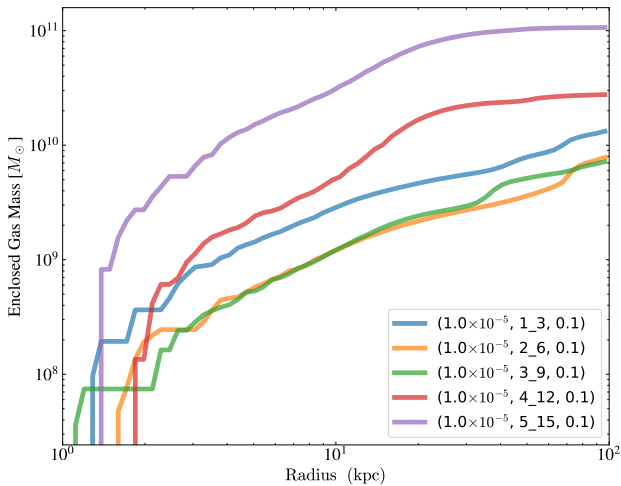


Figure 5. Cumulative plot of m_{gas} against halo radius. The different coloured lines represent simulations of various r and s . As the extent of feedback injection is increased beyond $r = 3$ and $s = 9$, the amount of baryons in the outer region of the halo is significantly higher. This trend highlights the inhibition of gas collapse to form stars as the extent increases, providing support for the explanation given in Section 4.1.1 for the trend in Figure 4.

versal baryon fraction while possessing f_s that is close to observations. These haloes are in contrast to the MW halo (rightmost red star), which hints at the need for additional modifications required to understand and determine if this discrepancy is a numerical byproduct due to the fractional mass resolution of the lower mass halo. Therefore, we attempt a zoom simulation of a dwarf galaxy around $10^{10} M_{\odot}$ with a comparable mass resolution to the MW zoom to investigate if the conclusion from Figure 7 is due to resolution and whether this feedback prescription is universal.

4.2 Dwarf galaxy zoom simulations with Setup 1

Using the combination of parameters $(2.5 \times 10^{-4}, 1.3, 0.2)$, we implement the feedback prescription in a dwarf galaxy with a mass of approximately $10^{10} M_{\odot}$. However, the results indicate an absence of stars within the halo, consistent with Figure 7. Reviewing the star formation routine (see Section 2.1), we find that the Jeans instability check is the bottleneck of star formation. Due to the spatial resolution implemented in this dwarf galaxy, according to the discussion in Section 2.1.1, the Jeans instability check restricts star formation that should occur in reality. Therefore, to allow star formation, we switch off this Jeans instability check in the star formation routine. We label such runs as NJ.

Figure 8 illustrates the virial (black) and stellar mass evolution (red) in the dwarf galaxy with different setups (solid vs dashed lines). As expected, removing the Jeans mass criterion allows stars to form in the dwarf galaxy zoom simulation (solid red line). However, star formation starts

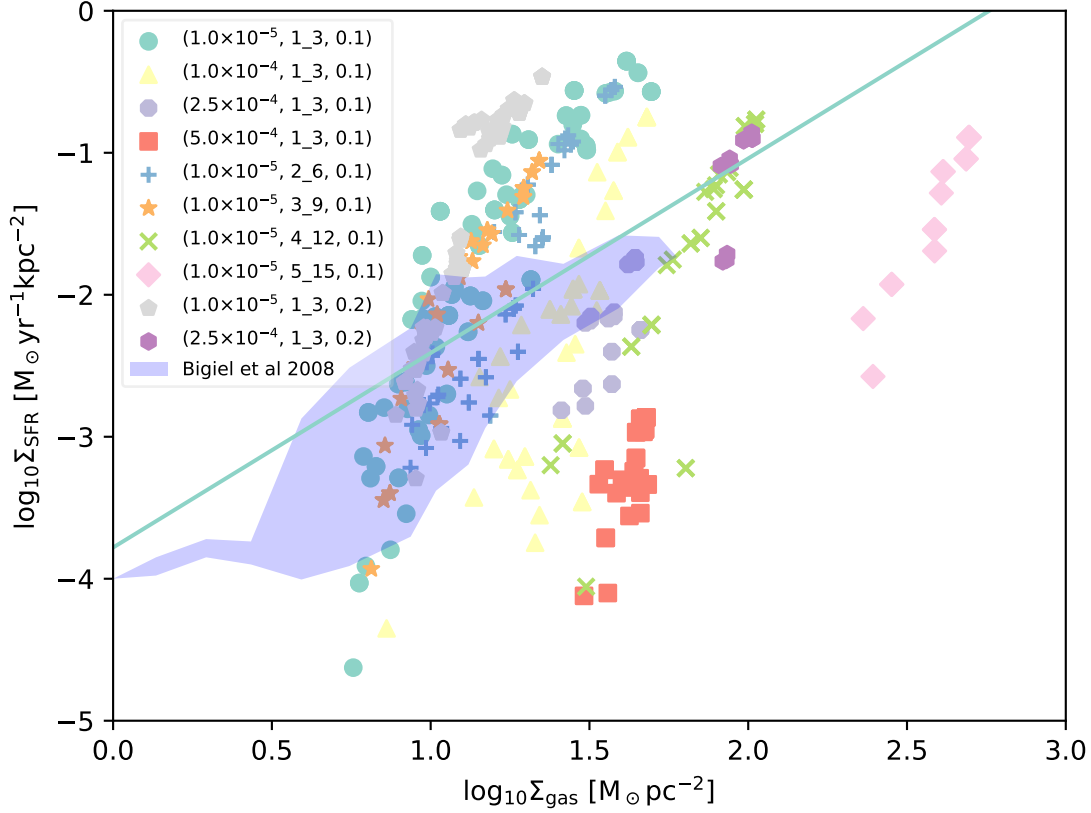


Figure 6. A graph of SFR surface density against gas surface density illustrating the KS relation. Different coloured points are simulation data from sub-kpc resolution consistent with rough approximation from the observations in nearby galaxies by Bigiel et al. (2008) represented by the blue hatched contours. The blue line is derived from the observational fit of Kennicutt et al. (2007). There is overlap between the simulation and observation but there are differences that will be discussed in Section 4.1.2.

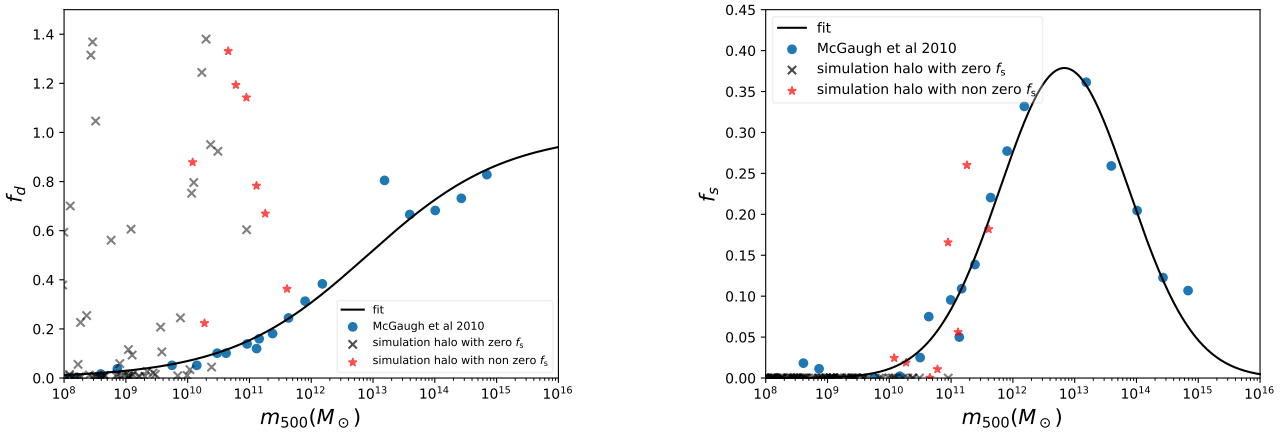


Figure 7. Graph of (a) the detected baryon fraction f_d against m_{500} and (b) the stellar mass fraction f_s against m_{500} with equations described in Section 3.1. The black line represents the fit given by Equation 10 and 11. The blue dots are points from McGaugh et al. (2010) and the crosses and stars are properties of haloes with various mass from the most refined region in the simulation. The black cross and red star refer to haloes in the must refine region with zero and non zero f_s respectively. Other than the most massive halo (MW halo), other haloes struggle to contain the appropriate amount of stars and gas. Refer to Section 4.1.3 for a detailed description.

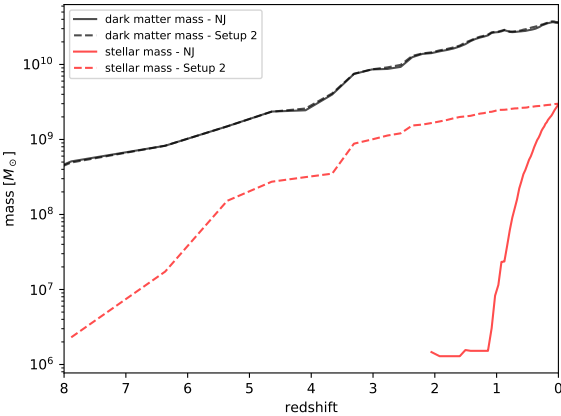


Figure 8. Redshift evolution of dark matter and stellar mass in the dwarf galaxy. Solid and dashed lines are mass evolution of NJ runs and Setup 2 runs respectively. Black lines refer to the dark matter mass evolution while red lines refer to the stellar mass evolution in the halo. By only switching off the Jeans instability check, the dwarf galaxy starts to form stars, albeit only at $z \approx 2$, which is too late. Therefore, we need a full transition to Setup 2 where the minimum star particle mass is set to zero in order to allow for star formation at an earlier time. Refer to Section 4.2 for discussion.

around $z = 2$, which is late as compared to the MW zoom simulation, for which star formation commenced at $z \approx 6.5$. Further investigations yielded the conclusion that the star formation threshold mass is the next limiting factor. Therefore, we reduce the threshold mass for star particle creation to zero, which relaxes the condition for star formation, allowing star particles to be created at $z = 8$ in the simulation. On top of these changes, we switch off the timestep dependence of star formation. This results in Setup 2 as shown in Table 1.

The purpose of $\Delta t/t_{\text{dyn}}$ in Equation 1 is to ensure the adherence of star formation to the KS relation. However, in Equation 3 where feedback is modelled to occur across time, there are additional factors of $\Delta t/t_{\text{dyn}}$ present to regulate these processes according to the KS relation. Hence, by switching to timestep independent star formation, we improve the promptness of the feedback. Lastly, since star formation is now instantaneous once conditions are met, high-density regions of gas are absent, reducing the time used to calculate the hydrodynamic evolution in the simulation. This absence of high-density gas is evident from the number of timesteps required for the evolution to reach $z = 0$ and the time per timestep. For an identical feedback prescription, Setup 1 takes 1263 timesteps and $\sim 435s$ per timestep to reach $z = 0$, which is in stark contrast to Setup 2 where it takes 663 timesteps and $\sim 125s$ per timestep for the simulation to reach $z = 0$. The net result is an improvement in the speed of completion of simulations from weeks to days.

In summary, we modify the setup to switch off the Jeans instability check, turn off the timestep dependence of star formation and remove the requirement of a minimum star particle mass. This results in Setup 2 shown in Table 1. This setup enables us to recover a more realistic star formation history beginning at $z \sim 8$ (see Figure 8), which is the main

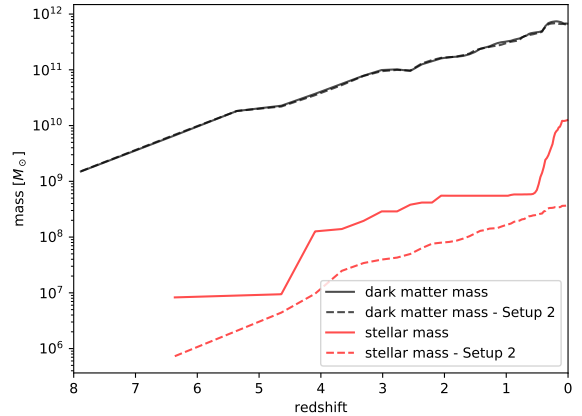


Figure 9. Redshift evolution of dark matter and stellar mass in the MW halo. Solid and dashed lines are mass evolution of NJ runs and runs with Setup 2 respectively. Black lines refer to the dark matter mass evolution while red lines look at the stellar mass evolution in the halo. By changing the star formation conditions, we obtain a smoother stellar mass evolution while not affecting the dark matter mass evolution. Refer to Section 4.3 for discussion.

motivation for the switch in setup. However, we do not compare the properties of the dwarf galaxy to observations for reasons that will be explained in Section 4.3.

4.3 Simulations with Setup 2

Due to star formation issues in the dwarf galaxy zoom simulations, we make significant changes in the simulation setup. In Section 4.2, we show that the stellar mass of a dwarf galaxy at $z = 0$ changed from zero to $\sim 10^9 M_{\odot}$ by switching to Setup 2. We now have to review the results of the MW galaxy presented in Section 4.1. Figure 9 shows the evolution of the dark matter and stellar mass of the MW halo in different setups. The lines and labels are similar to Figure 8.

From the identical dark matter mass evolution in Figure 9 for different setups (black lines), we know that we are comparing the same halo across simulations. However, the stellar mass evolution paints a different picture. Comparing both setups, although the haloes start forming stars at the same time ($z \approx 6.5$), the simulation using Setup 2 has a lower initial and final stellar mass as a result of its corresponding relaxed star formation conditions. With the minimum mass of the star particles set to zero, the stars are allowed to form with a smaller mass, which explains a lower starting point in Setup 2. Between $z = 1$ and $z = 0$ in Setup 1, we note a spike in stellar mass due to the build up of gas eligible for star formation (see Section 2.1.3). Despite these differences in the star formation history, the most significant one is the stellar mass of the halo at $z = 0$. The final stellar mass of the MW halo in Setup 1 is approximately $10^{10} M_{\odot}$, which is two orders of magnitude higher than that in the new run with a value of roughly $10^8 M_{\odot}$. This difference means that these haloes have vastly different f_{d} and f_{s} .

Due to the non-linear coupling of the various processes, changing individual prescriptions always requires new pa-

parameter fitting (Crain et al. 2015). With a new star formation setup, we have to re-explore the feedback parameter space with Setup 2. However, we have two distinct advantages as compared to before. The first is that we understand the general effects changing the feedback parameters have on the f_s and f_d of the halo (see Figure 4). Secondly, the simulations will complete much faster, allowing us to obtain more data points, both in general feedback parameter space and in the region around the best match to observations. This improvement will help us narrow down the feedback prescription, and possibly identify more than one combination that yields a close match. Obtaining more than one set of parameters will open up the possibilities of testing the robustness of the feedback prescription in the MW halo zoom simulations, haloes in the high-resolution region and the dwarf galaxy zoom simulations.

4.4 MW galaxy zoom simulations with Setup 2

We perform the following parameter space exploration with Setup 2 in Table 1. With this setup, we run a total of 49 simulations in order to calibrate the feedback prescription, and we make a similar classification as before, shown in Figure 3. We summarise the various properties of the halo of interest of simulations with Setup 1 and 2 in Table 3. This table includes simulations that will be discussed in Sections 4.5 and 4.6.

From the 49 simulations, only one simulation with $(3.0 \times 10^{-5}, 1.1, 1.0)$ failed to reach $z = 0$ due to the complete removal of gas when stars form. The process of iteration started from the best combination of parameters found in Section 4.1.1, $(2.5 \times 10^{-4}, 1.3, 0.2)$ and progressed based on the trends found in Figure 4 to move the simulation data point closer to the target. This process will be explained later. We introduce a measure of closeness between the simulated and the observed galaxy properties via the Cartesian distance to the target,

$$d = \sqrt{(f_{s(\text{sim})} - f_{s(\text{obs})})^2 + (f_{d(\text{sim})} - f_{d(\text{obs})})^2}, \quad (15)$$

where subscripts *sim* and *obs* refers to simulation and observation respectively. Lower values of d represent a more realistic simulated galaxy in terms of both f_s and f_d . For the goodness of fit of individual properties, we refer to Table 3.

Comparing the feedback parameter values covered in both Setup 1 and 2, it is clear that they do not cover an equal area of parameter space. The main differences lie in the usage of high f_* while having low values of r and ϵ in Setup 2 as compared to Setup 1. There are two significant volumes of parameter space not covered in Setup 2: large values of ϵ coupled with low r and f_* and large values of r with low values of ϵ and f_* . Also, there are regions (intermediate values of ϵ and f_* , high values of r and intermediate values of f_*) in the parameter space of Setup 2 that are not sampled. The reason why we do not have any simulations in these regions will be explained in the next section with Figure 10.

4.4.1 Comparison to Baryonic properties from McGaugh et al. (2010) – Setup 2

We will identify the best star formation and feedback parameters through an iterative process beginning from the initial point $(2.5 \times 10^{-4}, 1.3, 0.2)$ from before, applying the knowledge of trends from Figure 4. We use arrows to represent the general movement of data points due to the initial adjustments of f_* and ϵ before using r and s for the finer last adjustments on the f_s and f_d plane. We present this with a representative set of simulations in Figure 10, similar to Figure 4 by starting from the best combination of parameters (blue dot) in Setup 1. It is evident that identical feedback prescription in different settings produced a MW with disparate f_s and f_d . In Setup 2, the previously optimal values produced a MW galaxy with minimal stellar mass. This small amount of stars at $z = 0$ is a result of the relaxed star formation conditions producing numerous small star formation events, which instantly yield feedback and reduces future star formation.

From the starting point, we increase f_* from 0.2 to 0.9 (see green arrow in Figure 10). This trend indicates that as f_* increases, f_d decreases while f_s stays constant, which is in agreement with the combination of effects of the green and blue arrows shown in Figure 4. Despite only having two data points, we know from the direction given by the green arrow in Figure 4 that it will have the same effect on the properties as increasing ϵ (blue arrow). Therefore, if we increase f_* further in Figure 4, we can expect it to follow the last blue arrow, which is a horizontal motion of decreasing f_d with constant f_s . Together with the immediate feedback from stars, increasing f_* converts more gas into stars, which reduces the amount of gas, leading to the decline in f_d . Although more stars form initially, the feedback is stronger, reducing the amount of gas available to form more stars as the halo aged, resulting in a constant f_s . Therefore, we increase f_* in an attempt to move the data point as far left as possible in Figure 10 in preparation for the next step. The simulation with $f_* = 1.0$ does not produce a MW galaxy with significantly different f_s and f_d . Furthermore, this value of f_* caused the only failed run from 49 simulations. Hence, we settle on a f_* value of 0.9 (orange dot) as the starting point for the next phase of iteration.

After obtaining the minimal f_d with $(2.5 \times 10^{-4}, 1.3, 0.9)$, we attempt to increase f_s and f_d in the next iteration to move closer to the target. From what we have learned from Figure 4, we can achieve this by either decreasing ϵ or r . Since r is already at a minimum, lowering ϵ is the only option. We present only a representative set of data points connected by the blue arrows to illustrate the general change in f_s and f_d due to smaller ϵ values. This increase in f_s and f_d is in agreement with Figure 4, explained by the less efficient baryon expulsion, which leads to higher star formation and retention of gas within r_{500} .

The final step is to adjust r and s to improve the match to the observed f_s and f_d . Initially, we maintain the injection of feedback energy in a cube and increase the size, i.e. from $r = 1$ and $s = 3$ to $r = 2$ and $s = 6$. The aim is to obtain a point to the top right of the target and increase r and s correspondingly to move it towards the target as predicted by Figure 4. However, we do not obtain any good fit. Coupled with an upper limit to the extent of feedback

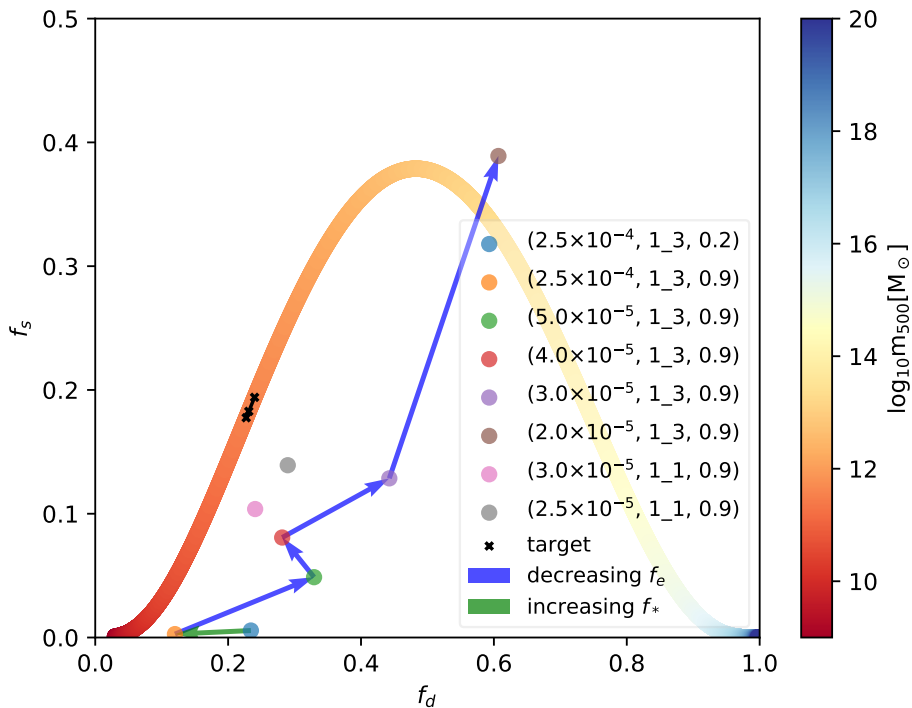


Figure 10. Graph of f_s against f_d across a range of m_{500} for Setup 2. The symbols and colour bar have the same meaning as those shown in Figure 4. The best combination of feedback parameter (blue dot) in Setup 1 no longer produces a realistic baryonic makeup of the MW halo. Instead, we have to re-calibrate the star formation and feedback prescription with the trends from Figure 4, resulting in $(2.5 \times 10^{-5}, 1_1, 0.9)$ and $(3.0 \times 10^{-5}, 1_1, 0.9)$ as the values required for Setup 2. For detailed description, we refer to Section 4.4.1.

injection where f_d increases instead beyond $r = 3$ and $s = 9$ (see Figure 4), we decide to change the shape of energy injection from a cube to just the adjacent cells centred around the star particle. In parameters terms, we change $r = 1$ and $s = 3$ to $r = 1$ and $s = 1$. As a result, the feedback energy is injected into four instead of 27 cells, effectively increasing the energy concentration per cell by approximately an order of magnitude. This increased energy density causes a larger decrease in f_d than in f_s . In contrast, increasing the extent of feedback injection maintained in a cube region generates a comparable change in both f_s and f_d .

We determine $(2.5 \times 10^{-5}, 1_1, 0.9)$ and $(3.0 \times 10^{-5}, 1_1, 0.9)$ as the two sets of parameters able to produce the smallest d value (see Table 3). Given the vast area of unexplored parameter space and the starting point of the iterative process, we justify that the steps taken constitute the most reasonable route through parameter space that can produce a close match to observations. The starting values of $(2.5 \times 10^{-4}, 1_3, 0.2)$ define the boundaries where values can be adjusted. r and f_* are almost at the minimum, meaning they can only increase while ϵ can either decrease or increase. Furthermore, the low f_s of the starting point of properties in Figure 10 suggests that the current feedback is too strong that it restricts star formation.

Together with the trends of changing parameters, the possible motions of the data point are a horizontal movement to the left or right, and diagonally right. The worst possible option is to increase ϵ , moving the data point to

the left. This choice leaves us stranded because we cannot create further motion since r and f_* are already close to their minimum values. The next possible option is to increase r above 3, causing the data to move horizontally right. The next steps associated with this first movement will be decreasing ϵ to iterate data points towards the top right before increasing f_* to reduce the data to match the target. However, given the initial movement away from the target, we believe that this will not produce a better match than what is presented. The most plausible option is to decrease ϵ , moving the data point along the blue arrows indicated in Figure 10. f_* can then be increased to move it down diagonally left towards the target while fine-tuning r and s . This change is preferred over increasing r because of the turn around expected beyond $r = 4$, which limits the degrees of freedom. However, following this option will generate a combination of parameters similar to what we have found. Out of the possible options to move the initial point in parameter space, we have chosen the path that will produce the best match to fit the observational data from [McGaugh et al. \(2010\)](#). Since the argument put forth does not mention the possibility of an ideal set of parameters lying in the region of parameter space consisting of intermediate values of ϵ and f_* and high values, they are not investigated.

Comparing the values of the feedback parameters that reproduce the MW baryonic makeup from both setups, we can identify the self-consistency of our feedback implementation. Setup 1 yielded an optimal combination of $(2.5 \times 10^{-4},$

Table 3. List of feedback prescriptions discussed in Sections 4.1, 4.4, 4.5 and 4.6 with the relevant properties of the halo of interest. These include m_{500} , $f_{\text{d}}(\text{obs})$, $f_{\text{d}}(\text{sim})$ and d as described in Section 4.4. The combination of feedback parameters that produces the lowest value of d , i.e., the most realistic galaxy in terms of its baryonic makeup is highlighted for each setup. We have included the sections in which each individual simulation is discussed, in order to guide the reader.

Feedback setup list							
MW galaxy zoom simulations – Setup 1							
Feedback parameters	$m_{500} [M_{\odot}]$	$f_{\text{d}}(\text{obs})$	$f_{\text{d}}(\text{sim})$	$f_{\text{s}}(\text{obs})$	$f_{\text{s}}(\text{sim})$	d	Discussed in Section
(1.0×10^{-5} , 1.3, 0.1)	5.59×10^{11}	0.26	1.41	0.22	1.25	1.54	4.1
(1.0×10^{-4} , 1.3, 0.1)	4.23×10^{11}	0.24	0.68	0.20	0.57	0.57	4.1
(2.5×10^{-4} , 1.3, 0.1)	4.92×10^{11}	0.25	0.82	0.21	0.42	0.60	4.1
(5.0×10^{-4} , 1.3, 0.1)	3.99×10^{11}	0.24	0.68	0.20	0.57	0.57	4.1
(1.0×10^{-3} , 1.3, 0.1)	3.88×10^{11}	0.24	0.19	0.19	6.01×10^{-3}	0.19	4.1
(1.0×10^{-5} , 2.6, 0.1)	4.65×10^{11}	0.25	1.02	0.20	0.91	1.04	4.1
(1.0×10^{-5} , 3.9, 0.1)	4.30×10^{11}	0.24	0.81	0.20	0.70	0.76	4.1
(1.0×10^{-5} , 4.12, 0.1)	5.05×10^{11}	0.25	0.86	0.21	0.54	0.69	4.1
(1.0×10^{-5} , 5.15, 0.1)	5.66×10^{11}	0.26	1.26	0.22	0.15	1.00	4.1
(1.0×10^{-5} , 1.3, 0.2)	5.53×10^{11}	0.26	1.37	0.22	1.22	1.49	4.1
(2.5×10^{-4} , 1.3, 0.2)	4.05×10^{11}	0.24	0.36	0.19	0.18	0.13	4.1
MW galaxy zoom simulations – Setup 2							
Feedback parameters	$m_{500} [M_{\odot}]$	$f_{\text{d}}(\text{obs})$	$f_{\text{d}}(\text{sim})$	$f_{\text{s}}(\text{obs})$	$f_{\text{s}}(\text{sim})$	d	Discussed in Section
(2.5×10^{-4} , 1.3, 0.2)	3.67×10^{11}	0.23	0.23	0.18	5.64×10^{-3}	0.17	4.4
(2.5×10^{-4} , 1.3, 0.9)	3.65×10^{11}	0.23	0.12	0.18	2.76×10^{-3}	0.21	4.4
(5.0×10^{-5} , 1.3, 0.9)	3.46×10^{11}	0.23	0.33	0.18	4.87×10^{-2}	0.16	4.4
(4.0×10^{-5} , 1.3, 0.9)	3.47×10^{11}	0.23	0.28	0.18	9.08×10^{-2}	0.11	4.4
(3.0×10^{-5} , 1.3, 0.9)	3.69×10^{11}	0.23	0.44	0.18	0.13	0.22	4.4
(2.0×10^{-5} , 1.3, 0.9)	4.15×10^{11}	0.24	0.61	0.19	0.39	0.42	
(3.0×10^{-5} , 1.1, 0.9)	3.50×10^{11}	0.23	0.24	0.18	0.10	7.59×10^{-2}	4.4 and 4.6
(2.5×10^{-5} , 1.1, 0.9)	3.71×10^{11}	0.23	0.29	0.18	0.14	7.3×10^{-2}	4.4 and 4.6
(3.0×10^{-5} , 1.1, 0.9) run 2	3.78×10^{11}	0.23	0.32	0.18	8.34×10^{-2}	0.14	4.6
(2.5×10^{-5} , 1.1, 0.9) run 2	3.59×10^{11}	0.23	0.33	0.18	0.15	0.10	4.6
Dwarf galaxy zoom simulations - Setup 2							
Feedback parameters	$m_{500} [M_{\odot}]$	$f_{\text{d}}(\text{obs})$	$f_{\text{d}}(\text{sim})$	$f_{\text{s}}(\text{obs})$	$f_{\text{s}}(\text{sim})$	d	Discussed in Section
(3.0×10^{-5} , 1.1, 0.9)	2.34×10^{10}	9.38×10^{-2}	8.14×10^{-2}	2.60×10^{-2}	8.47×10^{-3}	2.15×10^{-2}	4.5
(2.5×10^{-5} , 1.1, 0.9)	2.33×10^{10}	9.36×10^{-2}	0.12	2.58×10^{-2}	9.46×10^{-3}	2.79×10^{-2}	4.5

1.3, 0.2) but in Setup 2, we conclude that (2.5×10^{-5} , 1.1, 0.9) and (3.0×10^{-5} , 1.1, 0.9) reproduced the most realistic MW galaxy. In Setup 2, the simulation forms more star particles but they are of lower masses than in Setup 1. Therefore, in order to produce a similar amount of stars observed in a MW galaxy at $z = 0$, Setup 2 requires a higher gas to star conversion efficiency, 0.9 as compared to 0.2 in Setup 1. In response to this larger conversion efficiency, Setup 2 require a lower ϵ . The value of ϵ differs significantly between the setups as a result. Setup 2 is preferred because of the more realistic star formation history in the dwarf galaxy (see Section 4.2), and a more extensive exploration of parameter space due to higher computational resources efficiency.

4.4.2 Kennicutt–Schmidt relation – Setup 2

In this section, we will present the agreement of star formation in the simulation with the KS relation described in Section 3.2. As in Figure 6, we choose non-zero SFR patches within r_{500} at $z = 0$ and compare it to the fit given by Equation 14 and observations of nearby galaxies by Bigiel et al.

(2008), shown in Figure 11. There is a clustering of points around the fit but no slope can be deduced from the points. Also, the simulated gas density is too low for comparison to observational data. We believe the concentration of points around low surface gas density is due to the relaxed star formation criteria and the higher f_{s} . These conditions result in a more efficient conversion of gas into stars, leading to more feedback energy injection that lowers the gas density.

While (3.0×10^{-5} , 1.1, 0.9) and (2.5×10^{-5} , 1.1, 0.9) recovers f_{s} and f_{d} well, there is an absence of patches with high gas surface density, restricting our ability to probe the KS relation in that regime. This absence also suggests that feedback might have been too efficient in driving gas out of the central region of the galaxy. Comparing Setup 2 to Setup 1, the former is not as good in recovering the KS relation. Setup 2 provides a relatively more instantaneous conversion of gas into stars, which drives gas surface density to lower values. As discussed earlier, a larger quantity of stars is formed in Setup 2, which begins feeding back into the IGM immediately. Coupled with the high conversion ef-

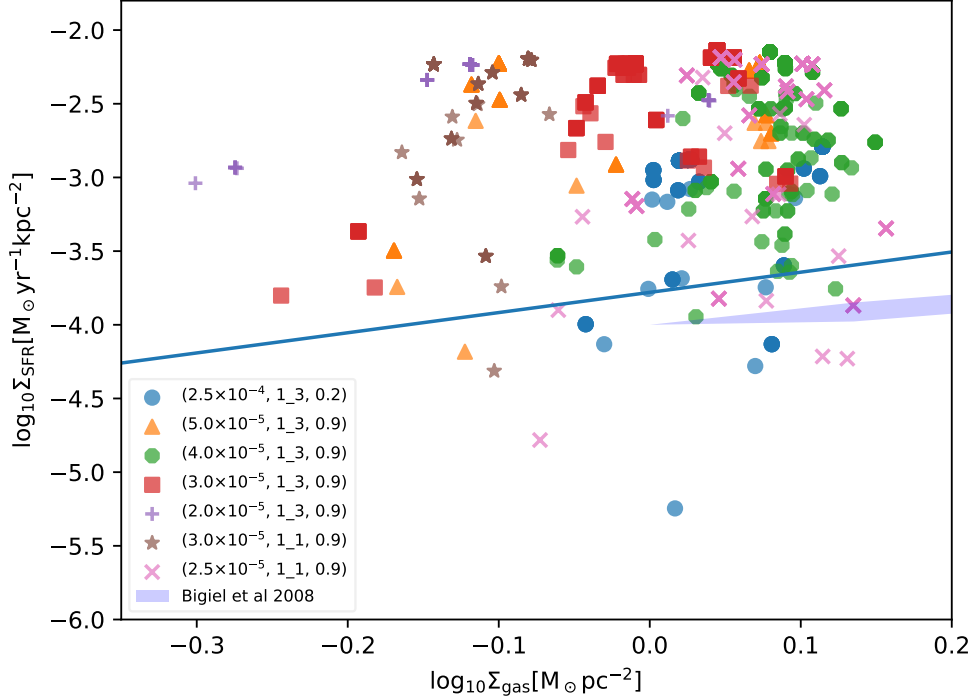


Figure 11. Graph of SFR surface density against gas surface density illustrating the KS relation as in Figure 6. Different coloured points are simulation data with sub-kpc resolution consistent with rough approximation from the observations in nearby galaxies by Bigiel et al. (2008) represented by the blue hatched contours. The blue line is derived from the observational fit of Kennicutt et al. (2007). As a result of the difference in the feedback prescription, the simulated galaxy have a much lower gas surface density as compared to Figure 6. For further description of this figure, we refer to Section 4.4.2.

efficiency of gas to stars, it empties the central region of the galaxy of gas, explaining why the gas surface density is low.

4.4.3 Haloes in the high-resolution region – Setup 2

As in Section 4.1.3, we look at the f_s and f_d of the other haloes within the high-resolution region of three virial radii from the MW halo. We plot f_d against m_{500} on the left column, f_s against m_{500} on the right column, and simulations with $(3.0 \times 10^{-5}, 1_1, 0.9)$ and $(2.5 \times 10^{-5}, 1_1, 0.9)$ on the top and bottom rows in Figure 12 respectively.

With the exception of one and two haloes from the runs with $(3.0 \times 10^{-5}, 1_1, 0.9)$ and $(2.5 \times 10^{-5}, 1_1, 0.9)$ respectively, we find very good agreement for both f_s and f_d of haloes between $10^{10} M_\odot$ and $10^{12} M_\odot$. This agreement is in contrast to Figure 7 where agreement is only achieved for f_s and not f_d . On top of that, the level of agreement with observations is much better in Figure 12 than Figure 7 as points lie closer to the fit. For haloes below $10^{10} M_\odot$, it is plausible that the lack of mass and spatial resolution is the cause of their inability to form stars. On the other hand, the larger mass haloes that suffer the same problem require future zoom simulations to be carried out in order to identify the root of the issue.

4.5 Dwarf galaxy zoom simulation with Setup 2

We conduct zoom simulations of a dwarf galaxy with m_{vir} of approximately $10^{10} M_\odot$ as an additional test of the universality of the feedback parameters in different halo mass bins. We described how we pick this dwarf galaxy from the high-resolution region of the MW zoom simulation in Section 2. Similarly, we increase the number of nested levels to keep the number of particles defining the halo constant with that of the MW while keeping the spatial resolution constant. We then compare the f_s and f_d of the halo to McGaugh et al. (2010) in Figure 13.

We present a close-up view of the parameter space in Figure 13 because we are showing results from zoom simulations of the dwarf galaxy using the two best sets of parameters only. It is clear that the f_s and f_d of the simulated galaxy in both feedback prescriptions are comparable to the target. We expect good agreement based on the results of Figure 12. Therefore, we argue that this feedback prescription is insensitive to mass resolution with a smaller mass halo having a lower and higher resolution in Figures 12 and 13 respectively. However, it is also essential to investigate the dependence of the feedback prescription on spatial resolution in future work.

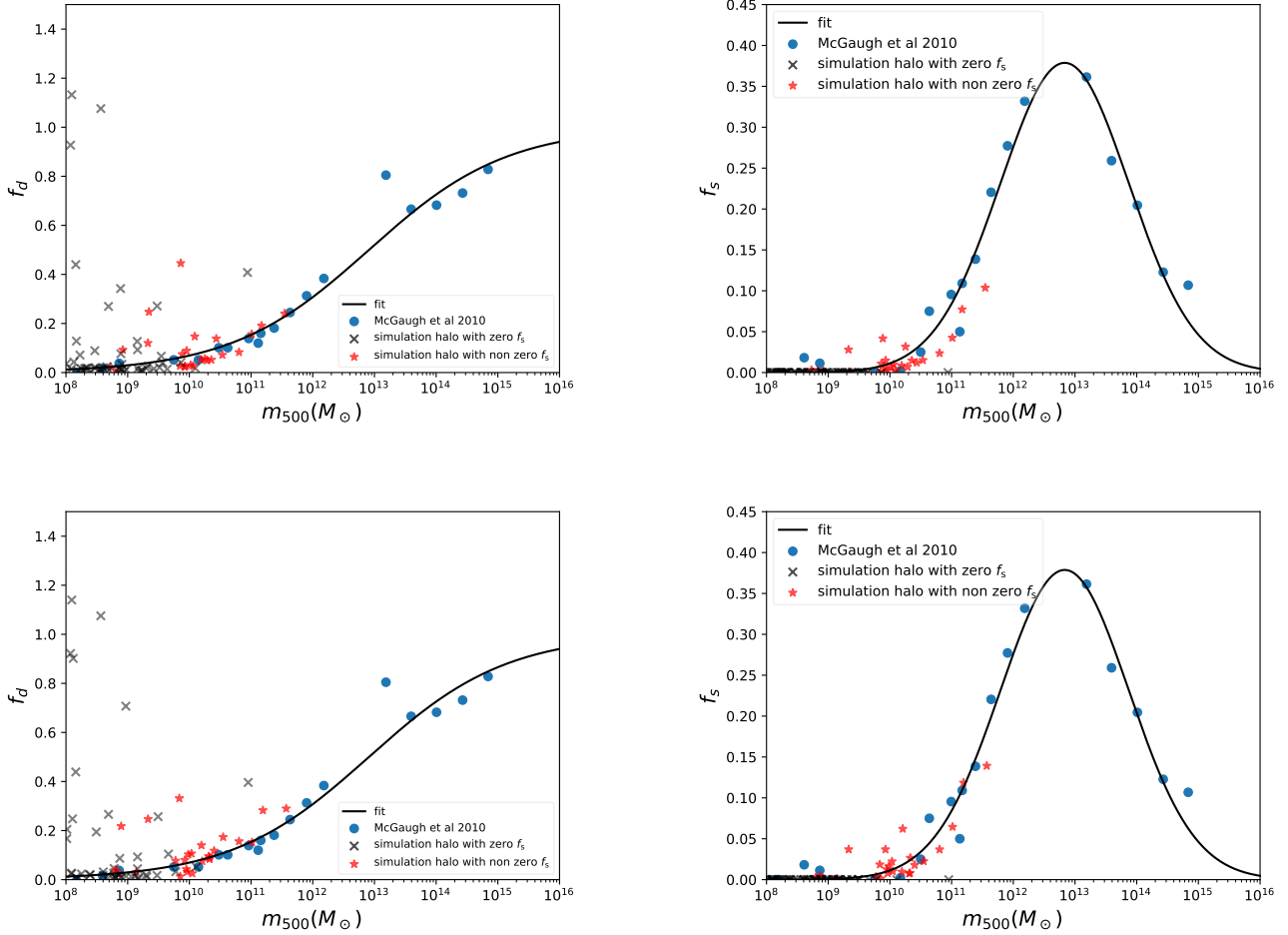


Figure 12. Graph of f_d against m_{500} (left) and f_s against m_{500} (right) with equations described in Section 3.1. The black line represents the fit given by Equation 10 and 11. The blue dots are data from McGaugh et al. (2010) while the crosses and stars are properties of haloes with various mass from the high-resolution region in the simulation. The black cross and red star refer to haloes in the must refine region with zero and non zero f_s respectively. Top row figures are from $(3.0 \times 10^{-5}, 1.1, 0.9)$ while the bottom row figures are from $(2.5 \times 10^{-5}, 1.1, 0.9)$. In contrast to the limited success illustrated in Setup 1 (see Figure 7), these feedback prescriptions in Setup 2 are able to reproduce the baryonic makeup in haloes between $10^{10} M_\odot$ and $10^{12} M_\odot$. Refer to Section 4.4.3 for a detailed description.

4.6 Chaos and variance

Recognising the argument put forth by Keller et al. (2019) for chaotic variance in numerical simulations, we conduct our zoom simulations twice on different processors. They have identical initial conditions and feedback prescriptions but evolved on different combinations of processors in the same computing cluster. The aim is to find out how much the halo properties would differ from each other due to the usage of a different set of processors. We quantify this difference in Figure 14.

Dots and stars in Figure 14 represent the pair of simulations with $(3.0 \times 10^{-5}, 1.1, 0.9)$ (blue) and $(2.5 \times 10^{-5}, 1.1, 0.9)$ (red) respectively. Despite both of them being close to the target, f_s and f_d for each pair can differ as much as running a simulation with a different set of feedback parameters. Comparing $(3.0 \times 10^{-5}, 1.1, 0.9)$ run 2 to $(4.0 \times 10^{-5}, 1.1, 0.9)$ in Figure 10, the simulated galaxies have similar values of f_s and f_d . This variance is also apparent from the values of

m_{500} where the maximum, minimum and the mean values are shown by the black crosses.

Looking at Figure 14, the deviation in f_s from the pair of simulations is comparable to the 10% difference in stellar mass concluded in Keller et al. (2019) despite not using identical processors. However, the deviation in total baryon mass is as high as 33%, possibly arising from the coupling of star formation and feedback where a 10% difference in stellar mass affects the feedback significantly. There is not a consistent trend observed in Figure 14, i.e., increase or decrease in f_s both cause an increase in f_d . We attribute this to these ratios containing a mixture of stellar and gas mass. Due to the complex coupling of star formation and feedback, it is difficult to disentangle the contribution of each component. For example, increasing stellar mass results in a decrease in gas mass but it is unclear which is the more dominant effect. As a result, the baryonic composition of the halo can differ drastically.

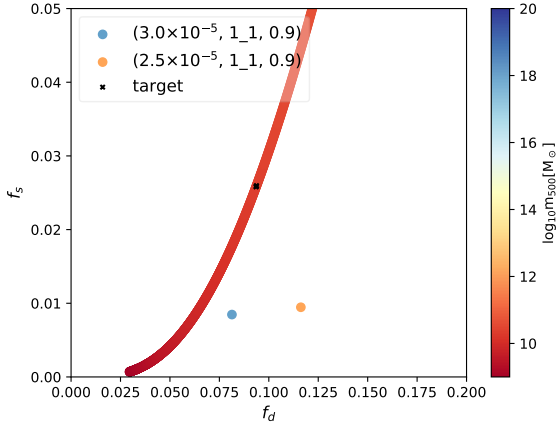


Figure 13. Plot of f_s against f_d for the zoom dwarf galaxy simulations. Various coloured dots represent runs with different set of feedback parameters with the colour bar having the usual meaning. It is focused on a small area near the target due to closeness of simulation results with the observed properties. Consistent with Figure 12, $(3.0 \times 10^{-5}, 1.1, 0.9)$ and $(2.5 \times 10^{-5}, 1.1, 0.9)$ are able to produce a dwarf galaxy with f_s and f_d close to observations. See Section 4.5 for a detailed description.

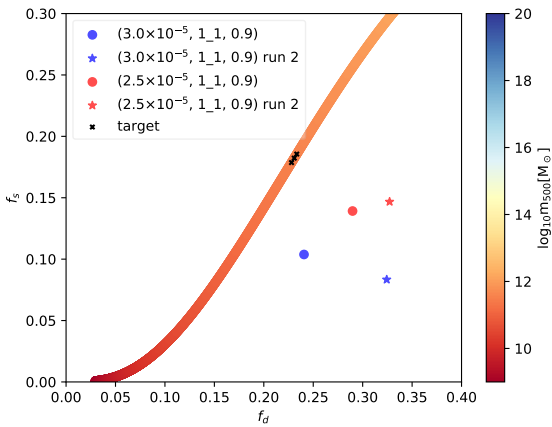


Figure 14. Plot of f_s against f_d for pairs on zoom MW simulation with identical initial conditions and feedback prescriptions evolved with different processors. The same coloured symbols refer to the simulations with identical setup while dots and stars represent identical simulations with two different sets of processors. The colour bar has its usual meaning. It is again focused in a small area near the target due to the level of agreement of simulation results with the properties. Rerunning a simulation with identical initial conditions can produce simulated properties that differ significantly. See Section 4.6 for a detailed description.

5 SUMMARY AND DISCUSSION

We present results from a large number of zoom simulations of both a MW and a dwarf galaxy. This suite of simulations is the first application of numerical simulations calibrated to match the baryon content and stellar fraction properties presented by [McGaugh et al. \(2010\)](#). Using the star formation routine of [Cen & Ostriker \(1992\)](#) and the thermal super-

nova feedback of [Cen & Ostriker \(2006\)](#), we select factors such as f_* to tune the conversion efficiency of gas to stars, ϵ for the feedback energy budget, and lastly, both r and s to calibrate the extent of feedback injection in the simulations. We also identify additional parameters that require adjustments in order to achieve realistic star formation histories. They are the Jeans instability check, the star particle threshold mass and the timestep dependence of star formation. These directly influence the criteria used to determine the occurrence of star formation.

It is remarkable that there is such a small variance associated with the data presented by [McGaugh et al. \(2010\)](#). This is the main reason why we strive to improve the agreement between our simulation results and observations as much as possible. However, it is also important to note the possibility of underestimates in the errors and unaccounted systematics. The method of determining the mass of the halo from observations affects the amount of scatter too. If abundance matching is used, m_* will have a lot more scatter than m_b in the Tully-Fisher plane at low mass, leading a corresponding amount of scatter in f_s and f_d . Since most of the mass in low mass rotating galaxies is gas and not stars, one can also question the applicability of extrapolating abundance matching relations to such low masses.

With the mentioned parameters, we produce a MW galaxy with realistic baryon and stellar fraction when compared to the observations of [McGaugh et al. \(2010\)](#) with our suite of simulations. We achieve this agreement with two different setups shown in Table 1. Setup 1 utilises a timestep dependent star formation with Jeans instability check and a star formation threshold mass of $10^5 M_\odot$. We attempt a total of 22 simulations with this setup and find that $(2.5 \times 10^{-4}, 1.3, 0.2)$ managed to reproduce the observed f_s and f_d . However, the simulated MW galaxy in this feedback prescription does not match the observed KS relation very well. By applying this feedback prescription to a zoom simulation of a dwarf in this setup, we find star formation starting too late as compared to the simulated MW galaxy. To resolve this issue, we propose switching to a timestep independent star formation setup with no Jeans instability check and threshold mass (Setup 2). However, due to the non-linear coupling of the various processes in the simulation, a new prescription requires re-exploration of subgrid parameters.

We begin an iterative process from $(2.5 \times 10^{-4}, 1.3, 0.2)$ in Setup 2, concluding with two sets of parameters that produced a close fit to the f_s and f_d with the use of 49 simulations. They are $(2.5 \times 10^{-5}, 1.1, 0.9)$ and $(3.0 \times 10^{-5}, 1.1, 0.9)$. As in Setup 1, there are issues with the KS relation of the simulated galaxy. However, these feedback prescriptions performed remarkably well in matching the baryonic makeup of haloes between $10^{10} M_\odot$ and $10^{12} M_\odot$ in the high-resolution region to observations. A perfect feedback prescription that is able to replicate all the observables in the universe does not exist. If the prescription is tuned to certain observables, it might fail to reproduce others, which then requires further iterations to the feedback implementation (e.g. [Pillepich et al. \(2018\)](#)).

The main difference between setups is the conditions for star formation, and this is reflected in the best values of the feedback parameters we find. In Setup 2, with more relaxed star formation criteria, f_* is high, and ϵ is low as compared to Setup 1. In Setup 2, star particles form with ease, of lower

mass but have a larger quantity. In order to match the same observed value of f_s with Setup 1, we use a higher value of f_* , creating star particles with higher mass. However, since we demand a good agreement with the observed f_d , we have to lower the feedback energy efficiency from these higher mass star particles. This adjustment results in a lower ϵ as compared to Setup 1. Therefore, combining the values of feedback parameters with the star formation criteria, we show the self-consistent characteristics of the feedback processes.

In Setup 2, the points coalesce around low gas surface density, with more gas being converted to stars due to the higher value of f_* and the relaxed star formation criteria. As a result, in the recovery of the KS relation in both simulation setups, Setup 2 did not perform as well as Setup 1. This inability to obtain an appropriate slope of the KS relation in both setups hints at a fundamental limitation of the [Cen & Ostriker \(1992\)](#) model. In terms of matching other observed properties, this feedback prescription requires more tuning or parameters.

Looking at the other haloes in the high-resolution region in Setup 2, all but three of the haloes within $10^{10} M_\odot$ and $10^{12} M_\odot$ with the calibrated star formation and feedback prescription are an excellent fit to f_s and f_d observed by [McGaugh et al. \(2010\)](#). In comparison to the results from Setup 1, the feedback prescriptions in Setup 2 perhaps suggest universality for haloes within the mass range described. We verify this claim with the zoom simulations of a dwarf galaxy of $10^{10} M_\odot$ with these feedback prescriptions. Through the haloes in the high-resolution region of the MW zoom simulation and the halo in the dwarf galaxy zoom simulation, we demonstrate the insensitivity of our feedback prescription on the mass resolution. However, we have to conduct the same test with much lower mass haloes as well as with different spatial resolutions. On top of the resolution, the universality and robustness of the feedback prescription should also be extended to galaxies with various star formation and merger history.

As we demonstrate, non-deterministic variance is a cause for concern; more computational resources need to be invested in order to understand, quantify and minimise these effects. Since we do not reproduce all the observational constraints mentioned, there exists the possibility of including more parameters in the feedback model or developing a different model. These should be the focus of future work to improve the feedback prescription in order for the simulated galaxies to better match observations.

ACKNOWLEDGEMENTS

BKO and JAP were supported by the European Research Council under grant number 670193. BKO would like to thank Jose Oñorbe and the TMOX group at the Royal Observatory, Edinburgh for many insightful discussions, and Daniele Sorini's various suggestions to improve the structure of the paper.

REFERENCES

Agertz O., Kravtsov A. V., Leitner S. N., Gnedin N. Y., 2013, *ApJ*, **770**, 25
 Behroozi P. S., Conroy C., Wechsler R. H., 2010, *ApJ*, **717**, 379

Behroozi P. S., Wechsler R. H., Wu H.-Y., 2013a, *ApJ*, **762**, 109
 Behroozi P. S., Wechsler R. H., Conroy C., 2013b, *ApJ*, **770**, 57
 Bennett C. L., et al., 2013, *ApJS*, **208**, 20
 Berger M. J., Colella P., 1989, *Journal of Computational Physics*, **82**, 64
 Bigiel F., Leroy A., Walter F., Brinks E., de Blok W. J. G., Madore B., Thornley M. D., 2008, *AJ*, **136**, 2846
 Blanchard A., Valls-Gabaud D., Mamon G. A., 1992, *A&A*, **264**, 365
 Booth C. M., Schaye J., 2009, *MNRAS*, **398**, 53
 Bower R. G., Benson A. J., Malbon R., Helly J. C., Frenk C. S., Baugh C. M., Cole S., Lacey C. G., 2006, *MNRAS*, **370**, 645
 Bryan G. L., et al., 2014, *ApJS*, **211**, 19
 Cen R., Ostriker J. P., 1992, *ApJ*, **399**, L113
 Cen R., Ostriker J. P., 2006, *ApJ*, **650**, 560
 Cole S., 1991, *ApJ*, **367**, 45
 Crain R. A., et al., 2015, *MNRAS*, **450**, 1937
 Dalla Vecchia C., Schaye J., 2012, *MNRAS*, **426**, 140
 Davé R., et al., 2001, *ApJ*, **552**, 473
 Davis A. J., Khochfar S., Dalla Vecchia C., 2014, *MNRAS*, **443**, 985
 Dekel A., Birnboim Y., 2006, *MNRAS*, **368**, 2
 Dekel A., Rees M. J., 1987, *Nature*, **326**, 455
 Diemand J., Kuhlen M., Madau P., Zemp M., Moore B., Potter D., Stadel J., 2008, *Nature*, **454**, 735
 Dubois Y., Teyssier R., 2008, *A&A*, **477**, 79
 Efstathiou G., Davis M., White S. D. M., Frenk C. S., 1985, *ApJS*, **57**, 241
 Enzo Collaboration 2018, Distributed Stellar Feedback, https://enzo.readthedocs.io/en/latest/physics/star_particles.html#distributed-feedback
 Ferland G. J., et al., 2013, *Rev. Mex. Astron. Astrofis.*, **49**, 137
 Gavazzi R., Treu T., Rhodes J. D., Koopmans L. V. E., Bolton A. S., Burles S., Massey R. J., Moustakas L. A., 2007, *ApJ*, **667**, 176
 Genel S., et al., 2018, preprint, ([arXiv:1807.07084](https://arxiv.org/abs/1807.07084))
 Giodini S., et al., 2009, *ApJ*, **703**, 982
 Governato F., et al., 2010, *Nature*, **463**, 203
 Griffen B. F., Ji A. P., Dooley G. A., Gómez F. A., Vogelsberger M., O'Shea B. W., Frebel A., 2016, *ApJ*, **818**, 10
 Haardt F., Madau P., 2012, *ApJ*, **746**, 125
 Hahn O., Abel T., 2011, *MNRAS*, **415**, 2101
 Heitmann K., Higdon D., White M., Habib S., Williams B. J., Lawrence E., Wagner C., 2009, *ApJ*, **705**, 156
 Hoekstra H., Hsieh B. C., Yee H. K. C., Lin H., Gladders M. D., 2005, *ApJ*, **635**, 73
 Hummels C. B., Bryan G. L., 2012, *ApJ*, **749**, 140
 Hummels C. B., et al., 2018, arXiv e-prints,
 Katz N., Gunn J. E., 1991, *ApJ*, **377**, 365
 Keller B. W., Wadsley J. W., Wang L., Kruijssen J. M. D., 2019, *MNRAS*, **482**, 2244
 Kennicutt Jr. R. C., 1989, *ApJ*, **344**, 685
 Kennicutt Jr. R. C., 1998, *ApJ*, **498**, 541
 Kennicutt Jr. R. C., et al., 2007, *ApJ*, **671**, 333
 Khochfar S., Ostriker J. P., 2008, *ApJ*, **680**, 54
 Kim J.-h., et al., 2016, *ApJ*, **833**, 202
 Klypin A. A., Trujillo-Gomez S., Primack J., 2011, *ApJ*, **740**, 102
 Komatsu E., et al., 2009, *ApJS*, **180**, 330
 Kravtsov A. V., 2013, *ApJ*, **764**, L31
 Madau P., Ferguson H. C., Dickinson M. E., Giavalisco M., Steidel C. C., Fruchter A., 1996, *MNRAS*, **283**, 1388
 Martizzi D., Teyssier R., Moore B., 2013, *MNRAS*, **432**, 1947
 McGaugh S. S., 2005, *ApJ*, **632**, 859
 McGaugh S. S., Schombert J. M., de Blok W. J. G., Zagursky M. J., 2010, *ApJ*, **708**, L14
 McKay M. D., Beckman R. J., Conover W. J., 1979, *Technometrics*, **21**, 239

- Moore B., Ghigna S., Governato F., Lake G., Quinn T., Stadel J., Tozzi P., 1999, *ApJ*, **524**, L19
- Moster B. P., Naab T., White S. D. M., 2013, *MNRAS*, **428**, 3121
- Navarro J. F., White S. D. M., 1994, *MNRAS*, **267**, 401
- Oñorbe J., Garrison-Kimmel S., Maller A. H., Bullock J. S., Rocha M., Hahn O., 2014, *MNRAS*, **437**, 1894
- Okamoto T., Eke V. R., Frenk C. S., Jenkins A., 2005, *MNRAS*, **363**, 1299
- Oppenheimer B. D., Davé R., 2006, *MNRAS*, **373**, 1265
- Ostriker J. P., Cowie L. L., 1981, *ApJ*, **243**, L127
- Peebles M. S., et al., 2019, *ApJ*, **873**, 129
- Pillepich A., et al., 2018, *MNRAS*, **473**, 4077
- Pontzen A., Governato F., 2012, *MNRAS*, **421**, 3464
- Schaye J., et al., 2010, *MNRAS*, **402**, 1536
- Schaye J., et al., 2015, *MNRAS*, **446**, 521
- Schmidt M., 1959, *ApJ*, **129**, 243
- Shimizu I., Todoroki K., Yajima H., Nagamine K., 2019, *MNRAS*, **484**, 2632
- Sijacki D., Springel V., Di Matteo T., Hernquist L., 2007, *MNRAS*, **380**, 877
- Simon J. D., Geha M., 2007, *ApJ*, **670**, 313
- Simpson C. M., Grand R. J. J., Gómez F. A., Marinacci F., Pakmor R., Springel V., Campbell D. J. R., Frenk C. S., 2018, *MNRAS*, **478**, 548
- Smith B. D., Hallman E. J., Shull J. M., O’Shea B. W., 2011, *ApJ*, **731**, 6
- Smith B. D., et al., 2017, *MNRAS*, **466**, 2217
- Smith M. C., Sijacki D., Shen S., 2018, *MNRAS*, **478**, 302
- Springel V., Hernquist L., 2003, *MNRAS*, **339**, 289
- Springel V., et al., 2008, *MNRAS*, **391**, 1685
- Stinson G., Seth A., Katz N., Wadsley J., Governato F., Quinn T., 2006, *MNRAS*, **373**, 1074
- Stone J. M., Norman M. L., 1992, *ApJS*, **80**, 753
- Storchi-Bergmann T., 2014, in Sjouwerman L. O., Lang C. C., Ott J., eds, *IAU Symposium Vol. 303, The Galactic Center: Feeding and Feedback in a Normal Galactic Nucleus*. pp 354–363 ([arXiv:1401.0032](https://arxiv.org/abs/1401.0032)), doi:10.1017/S174392131400091X
- Teyssier R., Moore B., Martizzi D., Dubois Y., Mayer L., 2011, *MNRAS*, **414**, 195
- Thacker R. J., Couchman H. M. P., 2000, *ApJ*, **545**, 728
- Turk M. J., Smith B. D., Oishi J. S., Skory S., Skillman S. W., Abel T., Norman M. L., 2011, *ApJS*, **192**, 9
- Vogelsberger M., et al., 2014, *MNRAS*, **444**, 1518
- Walker M. G., Mateo M., Olszewski E. W., Gnedin O. Y., Wang X., Sen B., Woodroffe M., 2007, *ApJ*, **667**, L53
- Walker M. G., Mateo M., Olszewski E. W., Peñarrubia J., Evans N. W., Gilmore G., 2009, *ApJ*, **704**, 1274
- Wang L., Dutton A. A., Stinson G. S., Macciò A. V., Penzo C., Kang X., Keller B. W., Wadsley J., 2015, *MNRAS*, **454**, 83
- White S. D. M., Frenk C. S., 1991, *ApJ*, **379**, 52

This paper has been typeset from a $\text{\TeX}/\text{\LaTeX}$ file prepared by the author.